

EXHIBIT DX5

TO DECLARATION OF PETER GOSS IN
SUPPORT OF DEFENDANTS' OPPOSITION
TO PLAINTIFFS' MOTION TO EXCLUDE
THE OPINIONS AND TESTIMONY OF
JOHN ABRAHAM, PH.D.

SIM SimCafe

SPACE SHORTCUTS

- Home
- ANSYS Learning Modules
- FLUENT Learning Modules
- ANSYS AIM Learning Modules
- BLADED Learning Modules
- MATLAB Learning Modules
- Creative Commons License

CHILD PAGES

- FLUENT - Sudden Expansion
 - Sudden Expansion - Verification ...



Space tools ▾

<<

Dashboard Spaces ▾

▢ ▾

Log in

for free online course on ANSYS

Pages / ... / FLUENT - Sudden Expansion

Sudden Expansion - Verification & Validation

Created by Sebastien Lachance-Barrett, last modified on Feb 13, 2014

Authors: Yong Wang & Said Elghobashi, UC Irvine

[Problem Specification](#)

1. Pre-Analysis & Start-Up
2. Geometry
3. Mesh
4. Physics Setup
5. Numerical Solution
6. Numerical Results
7. Verification & Validation

[Exercises](#)[Comments](#)

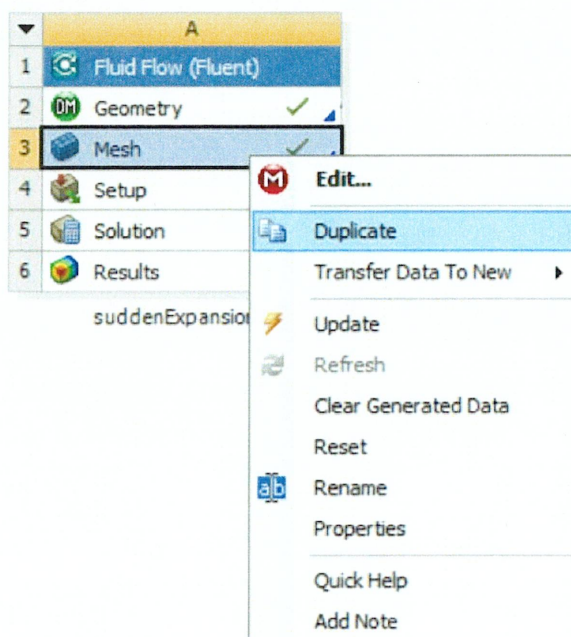
Verification and Validation

It is **very important** that you take the time to check the validity of your solution. Based on the velocity profile along the centerline, it can be seen that the max axis velocity in the small pipe is about $5.25e-1$ m/s. However, in a full-developed laminar pipe flow, the analytical max axis velocity should be two times of the uniform inlet velocity, that is $5.54e-1$ m/s. In other words, the results with the previous mesh are not good enough.

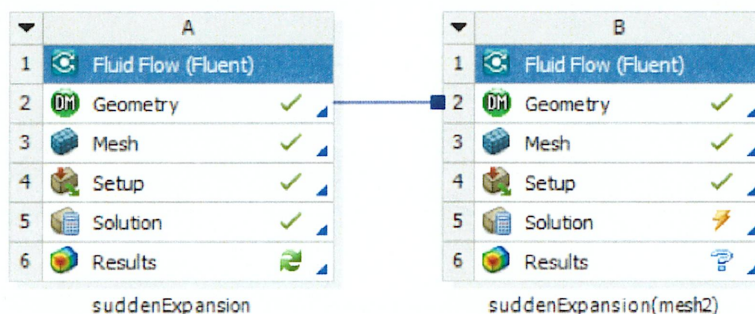
Refine Mesh

Let's repeat the solution on a finer mesh. For the finer mesh, the numbers of radial divisions will be twice as many as those used before. In the **Workbench Project Page** right click on **Mesh** then

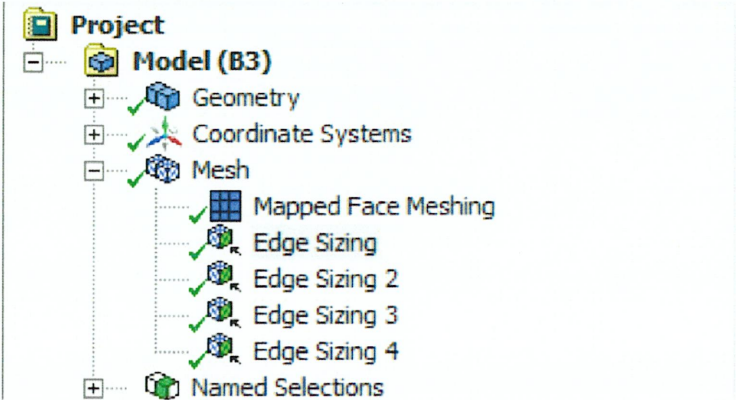
click **Duplicate** as shown below.



Rename the duplicate project to **suddenExpansion (mesh2)**. You should have the following two projects in your **Workbench Project Page**.



Next, double click on the **Mesh** cell of the **suddenExpansion (mesh2)** project. A new ANSYS Mesher window will open. Under **Outline**, expand **Mesh** and click on **Edge Sizing**, as shown below.



Here we will increase the numbers of cells in the radial direction. You may have different names of sizings. In my case, the "Edge Sizing" corresponds to the AB and EF edges, and "Edge Sizing 4" corresponds to the CD edge. Double the **Number of Divisions** of "Edge Sizing"

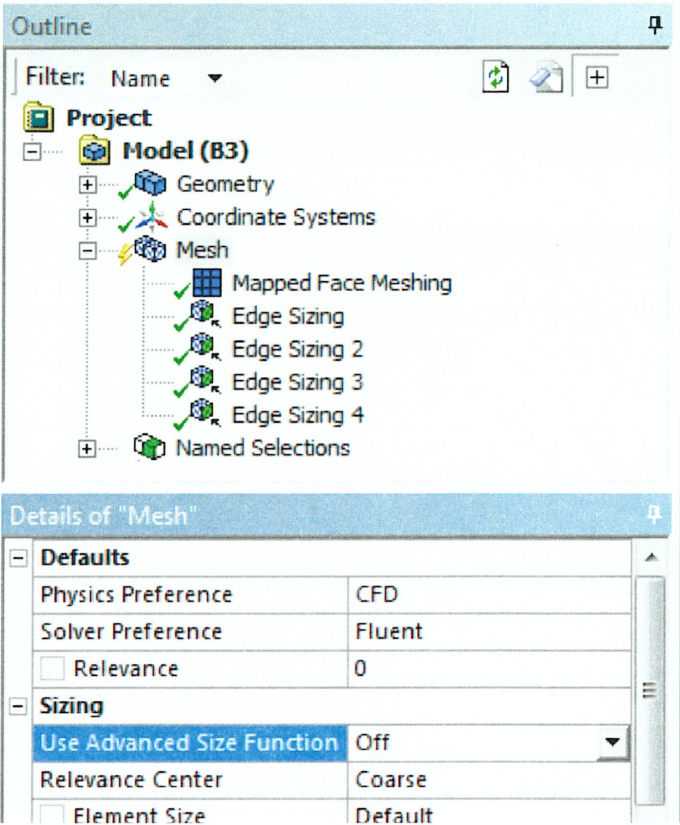
Details of "Edge Sizing" - Sizing	
Scope	
Scoping Method	Geometry Selection
Geometry	2 Edges
Definition	
Suppressed	No
Type	Number of Divisions
Number of Divisions	40
Behavior	Hard
Bias Type	No Bias

and "Edge Sizing 4"

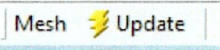
Details of "Edge Sizing 4" - Sizing	
Scope	
Scoping Method	Geometry Selection
Geometry	1 Edge
Definition	
Suppressed	No
Type	Number of Divisions
Number of Divisions	80
Behavior	Hard
Bias Type	No Bias

Sometimes, you need to turn-off **Advanced Size Function** under **"Details of Mesh"** to get the mesher to accept the modified settings. That way the Advanced Size Function feature will not over-

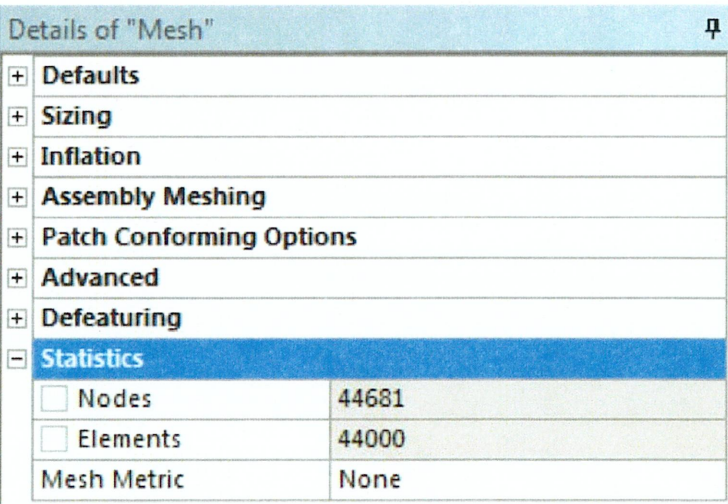
ride your settings (this feature is useful for meshing complex geometries). Click **Mesh** in the tree and turn off Advanced Size Function under "Details of Mesh" as shown below.



Then, click **Update** to generate the new mesh.

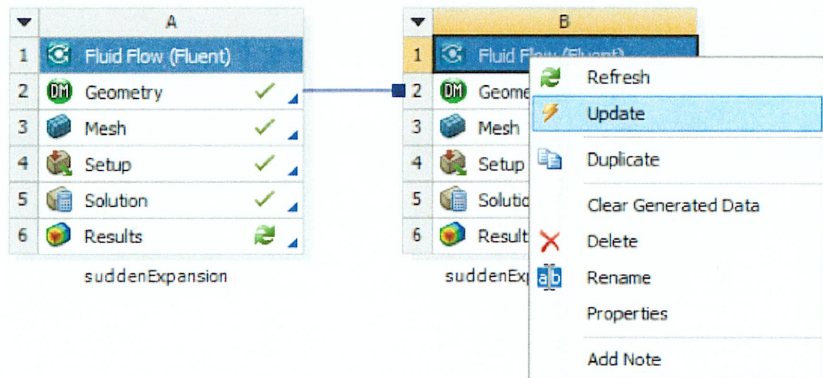


The mesh should now have 44000 elements. A quick glance of the mesh statistics reveals that there are indeed 44000 elements.



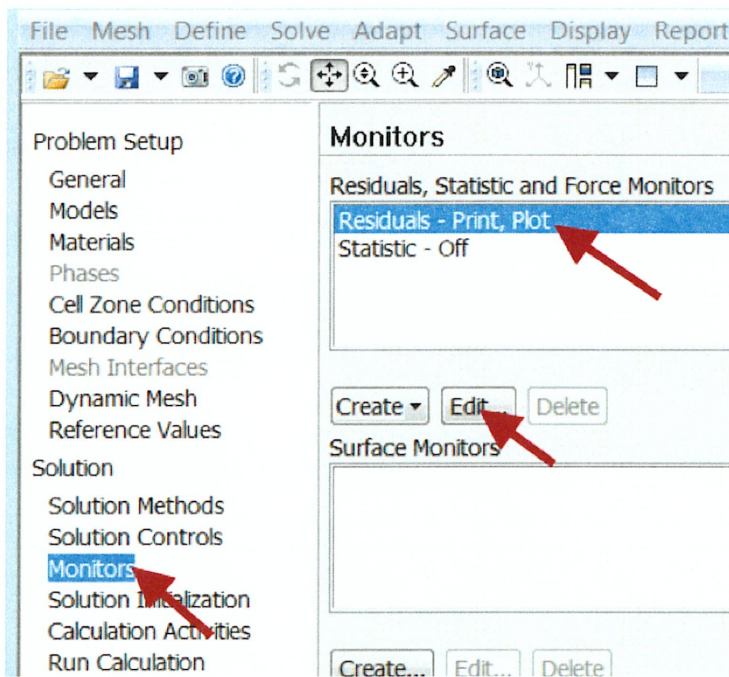
Compute the Solution

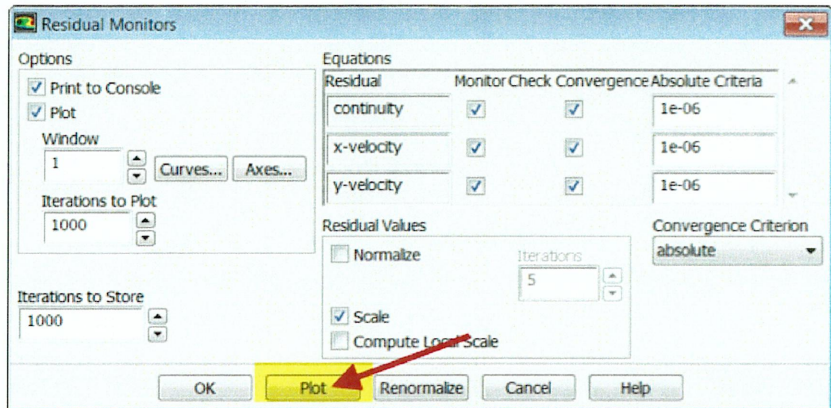
Close the ANSYS Mesher to go back to the **Workbench Project Page**. Under **suddenExpansion (mesh2)**, right click on **Fluid Flow (FLUENT)** and click on **Update**, as shown below.



Now, wait a few minutes for FLUENT to obtain the solution for the refined mesh. After FLUENT obtains the solution, save your project.

It is necessary to check that the solution iterations have converged. Launch FLUENT by double clicking on **Solution** of the "**suddenExpansion (mesh2)**" project in the **Workbench Project Page**. After FLUENT launches, select **Monitors > Residuals > Edit...** and then **Plot**, as shown in the images below.

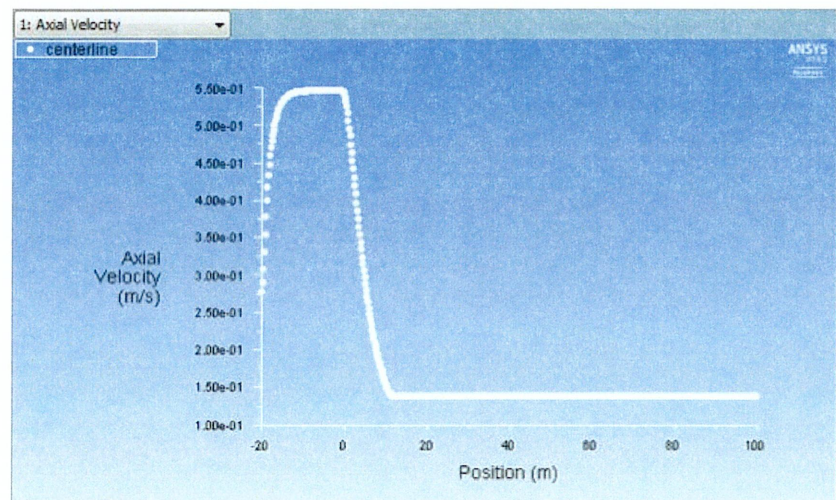




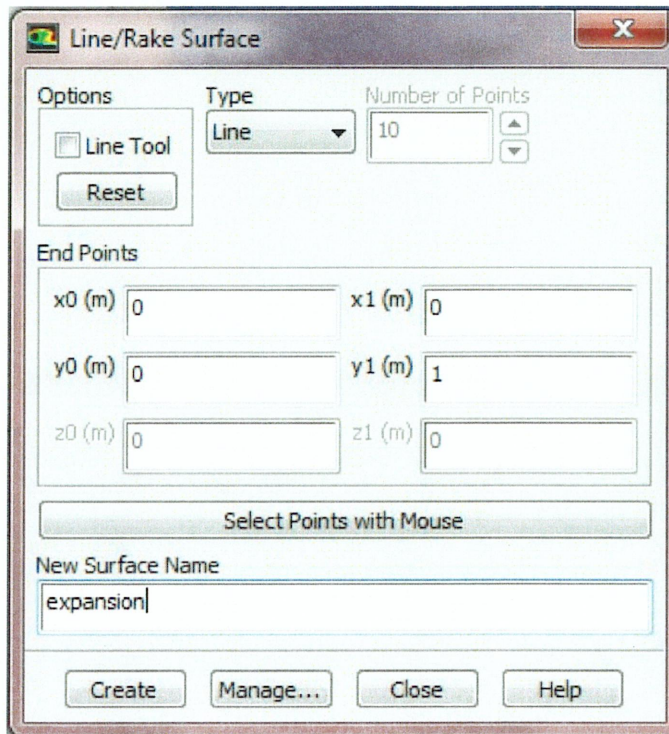
If the solution hasn't converged, one needs to run more iterations by selecting **Run Calculation**. You may want to increase the number of iterations. Ensure that you have a converged solution and save the project. Then, if you double-click on **Results** for mesh2 in the project page, you'll see that all results have been updated for the new mesh.

Velocity profile

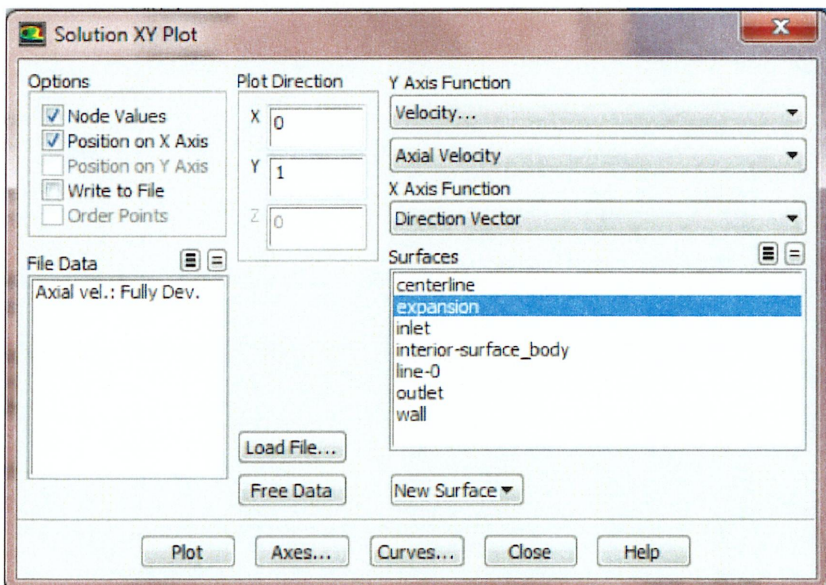
The plot below shows the profile of the axial velocity along the centerline ($y = 0$ m) with the refined mesh. It can be seen that the max velocity in the small pipe is about $5.50\text{e-}01$ m/s, which is close to the analytical solution ($5.54\text{e-}01$ m/s) and better than that of the previous mesh.



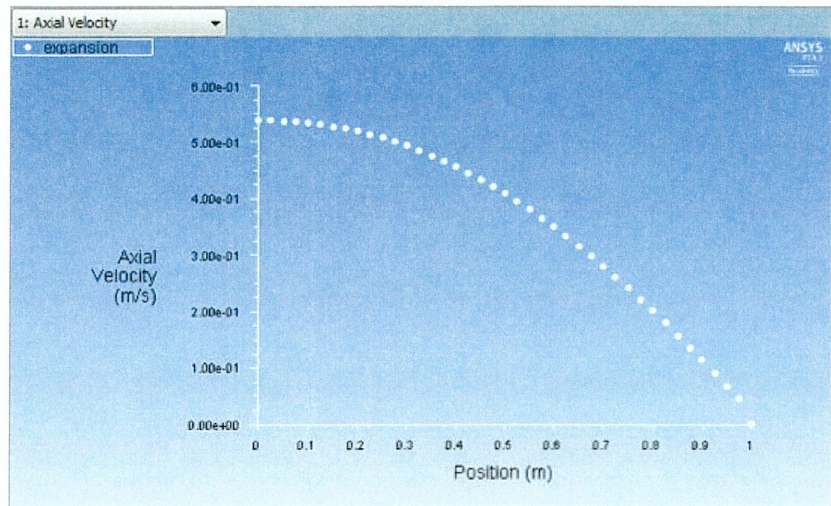
Here we will create a straight line for the expansion entrance, which is from $(x_0, y_0) = (0, 0)$ to $(x_1, y_1) = (0, 1)$. Select **Line** under **Surface**. Enter $x_0 = 0, y_0 = 0, x_1 = 0, y_1 = 1$. Enter **expansion** under **New Surface Name**. Click **Create**.



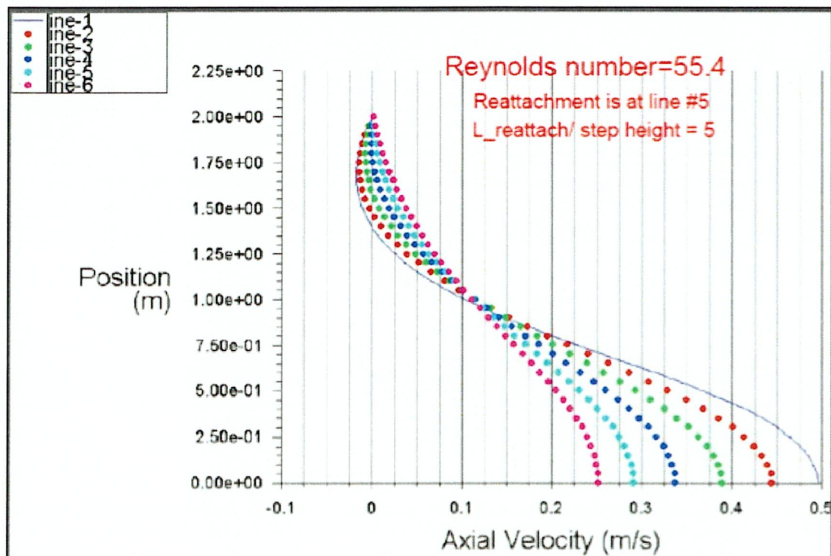
Then, plot the velocity profile along the **expansion** line. In the **Solution XY Plot** menu make sure that **Position on X Axis** is selected, and **X** is set to 0 and **Y** is set to 1.



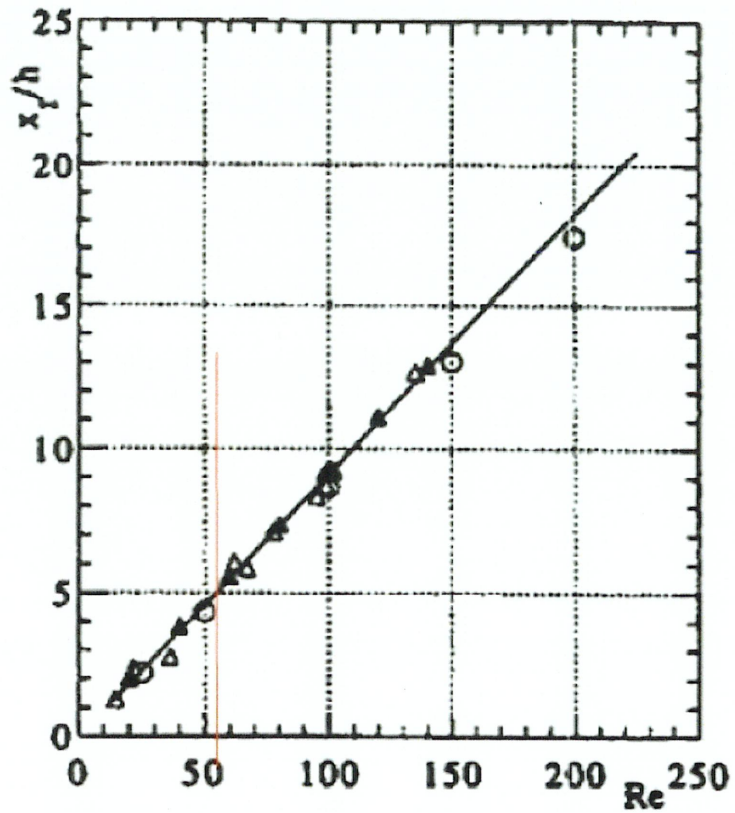
Then, click **Plot** and you should obtain the following output.



You can also plot axial velocity profiles at $x = 1$ m, 2 m, 3 m, 4 m, 5 m and 6 m as shown below. The numbers of the lines also indicate the distances from the expansion entrance to these lines.

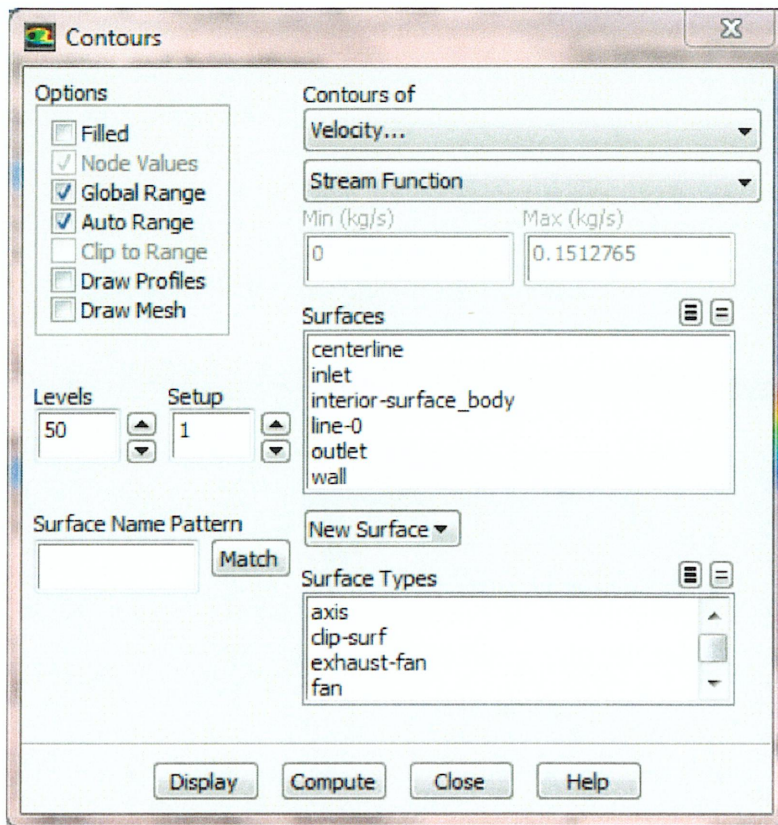


As you can see from the velocity profiles, the end of the recirculation region is at $x = 5$ m. In other words, the recirculation length for $Re = 55.4$ is about 5 times of the inlet radius, which agree well with the experimental data (*Hammad et al., Experiments in Fluids, 1999, 26:266-271*) shown below.

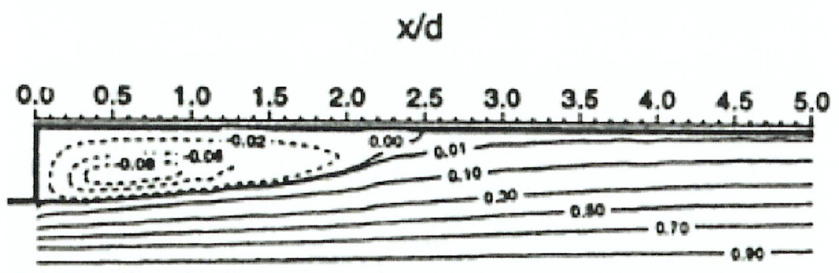
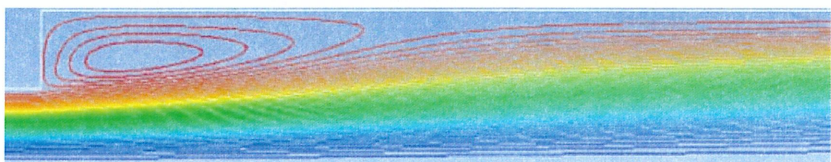


Streamline

First, click on **Graphics & Animations**. Next, double click on **Contours** which is located under **Graphics**. Select **Velocity** and **Stream Function** under **Contours of**, and change the number of **Levels** to 50, as shown below.



Then, click on **Display**. Zoom into the region near the expansion. The streamlines calculated with FLUENT are presented below, and compared with the streamlines obtained via PIV experiment (Hammad *et al.*, *Experiments in Fluids*, 1999, 26:266-271). It can be seen that the numerical result agree with the experiment one.



For more strict comparison, one should export the results from FLUENT, re-plot it in TECPLOT or some other post-processing software, and compare the value of stream function, redevelopment

length and recirculation length carefully. One can also increase the inlet velocity so that $Re = 200$, and then compare the results with experiment data presented in the reference.

[Go to Exercises](#)

[Go to all FLUENT Learning Modules](#)

Powered by Atlassian Confluence 5.8.18, Team Collaboration Software · [Report a bug](#)

[Atlassian News](#)

Numerical Heat Transfer, vol. 12, pp. 57-82, 1987

NUMERICAL SOLUTION OF LAMINAR FLOW PAST A SPHERE WITH SURFACE MASS TRANSFER

J. M. Conner and S. E. Elghobashi

*Department of Mechanical Engineering, University of California,
Irvine, California 92717*

The equations governing laminar flow past a sphere with surface mass transfer were solved numerically for low to moderate Reynolds numbers. The Reynolds number range considered was between 1 and 130. For mass transfer the Schmidt number was set equal to 1. Results of the calculations presented here include wake lengths, angles of separation, drag coefficients, and average Sherwood numbers. These predictions compare well with published experimental observations and other numerical results.

INTRODUCTION

Numerical solutions of the equations governing laminar flow over spheres are useful in understanding and mathematical modeling of dispersed multiphase flows. The numerical simulation of evaporating liquid droplets should, for example, benefit from a study of flow past a single sphere experiencing radial mass efflux from its surface.

This paper investigates this phenomenon by numerically predicting the flow around a sphere, using a modified version of the finite-volume method described by Patankar [1]. The modification concerns the use of an orthogonal curvilinear grid consisting of streamlines and potential lines for a potential flow around a sphere. The reason for selecting this particular grid system will be discussed below.

The effects of internal circulation in a liquid sphere on the surrounding flow field and on the mass transfer rate are briefly investigated by prescribing tangential surface velocity distributions obtained from the numerical work of Rivkind et al. [2].

In the course of this study we first predicted the laminar flow past a cylinder as a validation of the numerical method. Because of space limitations we present only a sample prediction of the cylinder flow.

The Reynolds number range investigated was 1 to 130. The lower limit of the Reynolds number was chosen because Stokes' approximate solution and Oseen's improvement are adequate below this limit due to the reduced significance of inertial effects. The upper limit was suggested by experimental observations indicating that, above the range considered, unsteady asymmetric oscillations of the wake region occur. All the flow fields studied here are assumed steady and symmetric.

The extensive literature concerning flow past spheres will not be reviewed in detail here. Instead, the reader is referred to Clift et al. [3], who have published a comprehensive review of numerical and experimental results related to flow past

The first author would like to thank Professor D. K. Edwards, Dr. A. Mostafa, and Dr. M. Rizk for helpful discussions during the course of this work.

NOMENCLATURE

A	matrix of the transformation	Sh_{ave}	average Sherwood number
a	sphere radius	U_i	parameter in the momentum equation
B_i	parameter in the momentum equation	U_∞	free-stream velocity
c, d	parameters	\mathbf{u}	velocity vector
C_D	drag coefficient	x_i	cartesian coordinate direction
C_f	friction drag coefficient	y_i	transformed coordinate direction
C_p	pressure drag coefficient	Γ	diffusion coefficient
D	sphere diameter	δ_{ij}	Kronecker delta
dA_{ij}	differential area	θ	polar angle
$d\mathbf{s}$	differential displacement vector	θ_s	angle of flow separation
ds	differential arc length	μ	fluid viscosity
dV	differential volume	μ^*	internal-to-external fluid viscosity ratio
\mathbf{e}_i	unit base vector	ρ	fluid density
\mathbf{F}	total flux vector	ϕ	velocity potential
F	drag force	Ψ	dimensionless stream function ($\Psi/U_\infty a^2$)
F_f	friction drag force	ψ	stream function
F_p	pressure drag force		
f	general dependent variable		
g_{ik}	Euclidean metric tensor		
h_i	geometric scale factor		
K, K'	Euclidean coordinate systems		
L	Length of the recirculating wake region		
m^*	dimensionless mass fraction		
m_i	mass fraction of species i		
p	pressure		
R	normalized polar radius (r/a)		
Re	Reynolds number ($\rho U_\infty D / \mu$)		
r	polar radius		
S	source per unit volume		
Sc	Schmidt number ($\mu / \rho \Gamma$)		
Sh_{loc}	local Sherwood number		
		Subscripts	
		ave	averaged over the surface of the sphere
		i	chemical species
		loc	local value corresponding to a point on the surface of the sphere
		s	evaluated at the surface of the sphere
		w, e, n, s	control volume faces
		∞	free-stream condition

spheres, including heat and mass transfer correlations. Some published numerical and experimental results that are significant for validating the present work are not mentioned in [3], however, and will be summarized here.

Rivkind and Ryskin [4] used a finite-difference technique to study the flow over liquid spheres for a broad range of internal-to-external fluid viscosity ratios. Modeling the interfacial boundary conditions allowed them to predict the stream function and vorticity distributions in both the external and internal flow fields. They presented streamline and vorticity contours and drag coefficients for external Reynolds numbers of 100 and 200. In a related paper, Rivkind et al. [2] presented computed drag coefficients and tangential surface velocity distributions for Reynolds numbers between 0.5 and 100 and viscosity ratios between 0 and 10. Their predicted surface velocity distributions for a Reynolds number of 100 and viscosity ratios of 0, 1, and 10 will be used here to investigate the effects of internal circulation on the mass transfer rates for the sphere.

Payard and Coutanceau [5] performed detailed flow visualization experiments

LAMINAR FLOW PAST A SPHERE

59

on spheres for Reynolds numbers between 10 and 60. They accurately determined the velocity distribution and other flow characteristics, such as wake length and angle of separation. Subsequently, Nakamura [6] performed flow visualization experiments for the sphere in this Reynolds number regime and found that a wake first appears at a Reynolds number as low as 7.3 and that the highest Reynolds number for a steady symmetric wake is about 190.

Available solutions of steady mass transfer of a chemical species from the surface of a sphere have considered the velocity-pressure fields as given or rather as independent of the mass transfer rate. Therefore, these solutions are valid only for low mass transfer rates. The effect of blowing from the sphere surface on the surrounding flow field was considered by Hamielec et al. [7], but the normal surface velocity distribution was assigned based on low mass transfer rate solutions. The present work intends to partially fill the gap in available solutions by predicting higher rates of mass transfer from spheres.

In the next section the governing equations, boundary conditions, and invoked assumptions will be described. Also, the reasons for choosing the particular coordinate system used in the numerical solution will be given. The numerical solution method will then be outlined. Finally, results of calculations performed for flow past a sphere will be presented.

MATHEMATICAL ANALYSIS

Choice of the Coordinate System

For computing the flow past a sphere with mass transfer, a set of elliptic partial differential equations describing the conservation of mass, momentum, and species concentration must be solved with the appropriate boundary conditions. The accuracy of the numerical solution of these equations is significantly improved when the flow boundaries coincide with those of the computational mesh. A most suitable mesh for the flow past a sphere is that consisting of the orthogonal net of streamlines and potential lines. Exact analytical expressions exist for the streamlines and potential lines of inviscid flow past a sphere, and thus these lines are chosen to construct the mesh for the present work. The details of the coordinate transformation used are given in the Appendix.

Governing Equations

The equations governing steady symmetric flow past a sphere will be presented in vector form and then, using the formulas of Brodkey [8], will be rewritten for component directions i , j , and k in orthogonal curvilinear coordinates. Here the transformed coordinate directions will be denoted by y with subscripts i and j being interchangeable and k referring to the azimuthal angle direction.

The continuity equation for a compressible steady flow is

$$\nabla \cdot (\rho \mathbf{u}) = 0 \quad (1a)$$

where ρ and \mathbf{u} are the fluid density and velocity vector, respectively. Equation (1a) may be expressed in orthogonal curvilinear coordinates as

$$\frac{1}{h_i h_j h_k} \left[\frac{\partial}{\partial y_i} (h_j h_k \rho u_i) + \frac{\partial}{\partial y_j} (h_i h_k \rho u_j) \right] = 0 \quad (1b)$$

where the h_i 's are the scale factors defined in the Appendix.

The equation for conservation of a chemical species l , where m_l is the mass fraction of species l and Γ is the mass diffusion coefficient, is

$$\nabla \cdot (\rho \mathbf{u} m_l) = \Gamma \nabla^2 m_l \quad (2a)$$

and in orthogonal curvilinear coordinates is

$$\begin{aligned} & \frac{1}{h_i h_j h_k} \left[\frac{\partial}{\partial y_i} (h_j h_k \rho u_i m_l) + \frac{\partial}{\partial y_j} (h_i h_k \rho u_j m_l) \right] \\ &= \frac{\Gamma}{h_i h_j h_k} \left[\frac{\partial}{\partial y_i} \left(\frac{h_j h_k}{h_i} \frac{\partial m_l}{\partial y_i} \right) + \frac{\partial}{\partial y_j} \left(\frac{h_i h_k}{h_j} \frac{\partial m_l}{\partial y_j} \right) \right] \end{aligned} \quad (2b)$$

The equation for conservation of momentum, where p is the pressure and μ is the fluid viscosity, is

$$\nabla \cdot (\rho \mathbf{u} \mathbf{u}) = -\nabla p + \mu \nabla^2 \mathbf{u} \quad (3a)$$

The expansion of the vector equation for momentum conservation into orthogonal curvilinear coordinates is given in [8]. For the two-dimensional axisymmetric geometry considered here, Brodkey's expression [8] for the representative component direction i reduces to

$$\nabla \cdot (\rho \mathbf{u} u_i) + \rho U_i = -\frac{1}{h_i} \frac{\partial p}{\partial y_i} + \mu \nabla^2 u_i + \mu B_i \quad (3b)$$

where

$$\nabla \cdot (\rho \mathbf{u} u_i) = \frac{1}{h_i h_j h_k} \left[\frac{\partial}{\partial y_i} (h_j h_k \rho u_i u_i) + \frac{\partial}{\partial y_j} (h_i h_k \rho u_j u_i) \right] \quad (3c)$$

$$\nabla^2 u_i = \frac{1}{h_i h_j h_k} \left[\frac{\partial}{\partial y_i} \left(\frac{h_j h_k}{h_i} \frac{\partial u_i}{\partial y_i} \right) + \frac{\partial}{\partial y_j} \left(\frac{h_i h_k}{h_j} \frac{\partial u_i}{\partial y_j} \right) \right] \quad (3d)$$

$$U_i = -\frac{u_j^2}{h_i h_j} \frac{\partial h_j}{\partial y_i} + \frac{u_i u_j}{h_i h_j} \frac{\partial h_i}{\partial y_j} \quad (3e)$$

and

$$\begin{aligned} B_i = & -\frac{u_j}{h_j^2 h_i h_k} \frac{\partial h_j}{\partial y_i} \frac{\partial h_k}{\partial y_j} + \frac{u_i}{h_i h_j^2 h_k} \frac{\partial h_i}{\partial y_j} \frac{\partial h_k}{\partial y_j} - \frac{u_j}{h_j} \frac{\partial}{\partial y_j} \left(\frac{1}{h_i h_j} \frac{\partial h_j}{\partial y_i} \right) \\ & + \frac{u_i}{h_j} \frac{\partial}{\partial y_j} \left(\frac{1}{h_i h_j} \frac{\partial h_i}{\partial y_j} \right) + \frac{u_i}{h_i} \frac{\partial}{\partial y_i} \left(\frac{1}{h_i h_k} \frac{\partial h_k}{\partial y_i} \right) + \frac{u_i}{h_i} \frac{\partial}{\partial y_i} \left(\frac{1}{h_i h_j} \frac{\partial h_j}{\partial y_i} \right) \end{aligned}$$

LAMINAR FLOW PAST A SPHERE

61

$$\begin{aligned}
& + \frac{u_i}{h_i} \frac{\partial}{\partial y_i} \left(\frac{1}{h_i h_j} \frac{\partial h_i}{\partial y_j} \right) + \frac{u_j}{h_i} \frac{\partial}{\partial y_i} \left(\frac{1}{h_j h_k} \frac{\partial h_k}{\partial y_j} \right) + \frac{2}{h_i} \frac{\partial u_j}{\partial y_j} \frac{\partial}{\partial y_i} \left(\frac{1}{h_j} \right) \\
& - \frac{2}{h_j} \frac{\partial u_i}{\partial y_i} \frac{\partial}{\partial y_j} \left(\frac{1}{h_i} \right) + \frac{1}{h_i} \frac{\partial u_i}{\partial y_i} \frac{\partial}{\partial y_i} \left(\frac{1}{h_i} \right)
\end{aligned} \quad (3f)$$

The stream function ψ for axisymmetric curvilinear coordinates may be defined by using the continuity equation for incompressible flow, given as

$$\frac{\partial}{\partial y_i} (h_j h_k u_i) + \frac{\partial}{\partial y_j} (h_i h_k u_j) = 0 \quad (4)$$

The function $\psi(y_i, y_j)$, which identically satisfies Eq. (4), is then

$$u_i = \frac{1}{h_j h_k} \frac{\partial \psi}{\partial y_j} \quad (5a)$$

and

$$u_j = - \frac{1}{h_i h_k} \frac{\partial \psi}{\partial y_i} \quad (5b)$$

Finally, combining Eqs. (5a) and (5b) gives

$$d\psi = u_i h_j h_k dy_j - u_j h_i h_k dy_i \quad (6)$$

Boundary Conditions

Referring to Fig. 1, the boundaries of the computational domain are located as follows. The upstream or left boundary is 10 diameters from the stagnation point, while the downstream and free-stream boundaries are 20 diameters from the surface of the sphere, respectively. The following boundary conditions were prescribed:

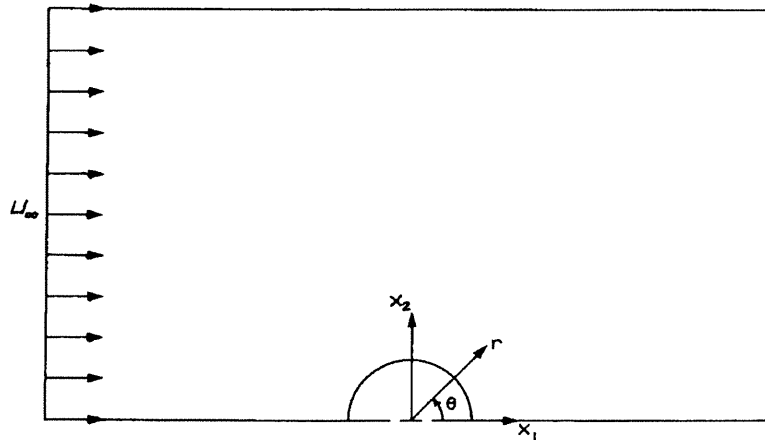


Fig. 1 Geometry of the flow field.

1. Velocity components $u_1 = U_\infty$ and $u_2 = 0$ at the left boundary.
2. The gradient in the x_1 direction of all dependent variables is zero at the right boundary.
3. The gradient in the x_2 direction of all dependent variables is zero at the upper boundary and the axis of symmetry.
4. The velocity component u_2 is zero at the axis of symmetry.
5. The velocity vector \mathbf{u} is specified at the solid boundary.

In the case of mass transfer from the surface of the sphere, the mass fraction of the evaporating species m_l is set to zero at the left boundary and is specified at the solid boundary. Also, it can be shown using the vapor conservation equation at the sphere's surface, that

$$u_{2,s} = - \frac{\Gamma}{1 - m_{l,s}} \frac{1}{h_2} \left(\frac{\partial m_l}{\partial y_2} \right)_s \quad (7)$$

The boundary condition expressed by Eq. (7) will be used to model the effects of mass transfer on the surrounding flow field.

NUMERICAL PROCEDURE

Integration of the Conservation Equations in Transformed Coordinates

The numerical procedure used to integrate the governing equations is an adaptation of the one described by Patankar [1], adapted to accommodate axisymmetric orthogonal curvilinear coordinates.

The general equation for the transport of a dependent variable f is

$$\nabla \cdot (\rho \mathbf{u} f) = \nabla \cdot (\Gamma \nabla f) + S \quad (8)$$

where ρ is the fluid density, \mathbf{u} the velocity vector, Γ the diffusion coefficient, and S the source per unit volume. For the mass transfer equation, f is taken to be the mass fraction m_l of species l , Γ is the diffusion coefficient, and S is zero. For the momentum equation, f is taken to be a velocity component, u_i , Γ is the fluid viscosity μ , and S is taken as

$$S = - \frac{1}{h_i} \frac{\partial p}{\partial y_i} - \rho U_i + \mu B_i \quad (9)$$

The aim of the numerical method is to obtain values of the dependent variables at discrete grid points. The equations that determine these values are derived by integrating Eq. (8) over a finite control volume surrounding each grid point. A typical control volume is shown in Fig. 2 for an orthogonal curvilinear coordinate system.

Let \mathbf{F} denote the total flux vector, given as

$$\mathbf{F} = \rho \mathbf{u} f - \Gamma \nabla f \quad (10)$$

Substituting Eq. (10) into Eq. (8) gives

LAMINAR FLOW PAST A SPHERE

63

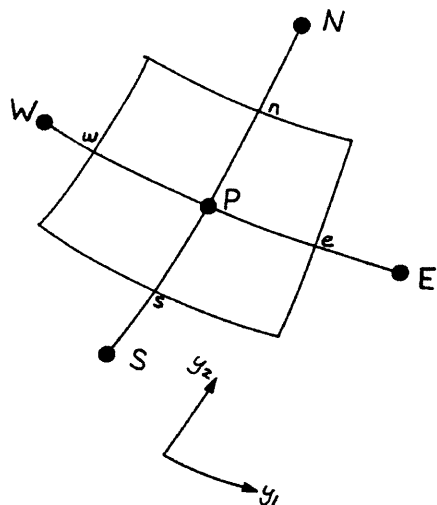


Fig. 2 Typical control volume in curvilinear coordinates.

$$\nabla \cdot \mathbf{F} = S \quad (11)$$

Using notation similar to that in [1], the integration of Eq. (11) over the control volume shown in Fig. 2 leads to

$$F_w A_w - F_e A_e + F_s A_s - F_n A_n = S_v \Delta V \quad (12)$$

Here the F 's represent the appropriate total fluxes at the control volume faces, the A 's are the corresponding areas, S_v is the source term averaged over the control volume, and ΔV is the volume of the control volume.

The iterative computational procedure solves Eq. (12) for every control volume in the solution domain until a converged solution is obtained. The remaining details of the numerical procedure may be found in references [1] and [9].

Method for Generating the Computational Grid

The computational grid, which consists of an orthogonal net of streamlines and potential lines, is generated by calculating the coordinates (x_1, x_2) of a node that corresponds to a point in the transformed flow domain whose coordinates (y_1, y_2) are known. The formulas relating (x_1, x_2) to (y_1, y_2) are given in the Appendix. A computer program was developed to plot the grid in physical space, using a set of (y_1, y_2) coordinates as input. Several grids of different densities could then easily be generated by using this program interactively. To calibrate the grid density, calculations were performed on a number of grids for a Reynolds number of 40. The grid fineness was then increased until the predicted angle of flow separation and wake length were within 2% of the measured values for this Reynolds number. The grid shown in Fig. 3 met this criterion.

RESULTS AND DISCUSSION

Flow past a Sphere

Calculations were performed for a flow past a sphere, using the grid displayed in Fig. 3. The Reynolds number varied from 1 to 130. The grid used was 83 divisions

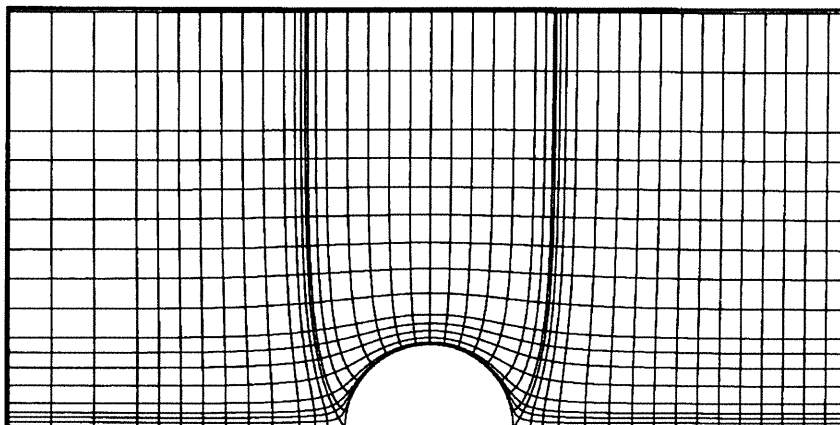


Fig. 3 Streamline-potential line grid used for computing the flow past a sphere.

in the streamwise direction (or in the velocity potential coordinate) and 31 divisions in the direction perpendicular to the flow (or in the stream function coordinate). A nonuniform grid spacing was used to allow finer resolution near the surface of the sphere. A typical computational time was about 1.5 h of CPU time on a VAX 11/780 computer.

From the converged velocity distributions, the variation of the stream function ψ over the flow field was computed. For the purpose of comparing the predictions for different Reynolds numbers, we define the dimensionless stream function Ψ as

$$\Psi = \frac{\psi}{U_{\infty} a^2} \quad (13)$$

where a is the sphere radius. Streamlines (contours of Ψ) for a Reynolds number of 100 are shown in Fig. 4, where the appearance of a standing pair of symmetric eddies



Fig. 4 Streamlines for flow past a sphere, $Re = 100$. Values of the dimensionless stream function Ψ are shown for selected contours. Values of Ψ for the recirculating wake region are given as follows, starting from the center: $\Psi = -0.01, -0.0051, -0.0021$.

LAMINAR FLOW PAST A SPHERE

65

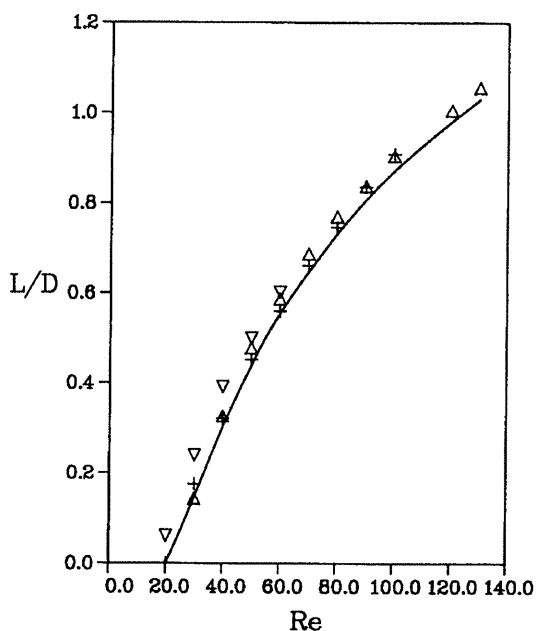


Fig. 5 Variation of wake length with Reynolds number for the sphere. The present results (solid curve) are compared with the experimental data of (Δ) Taneda [10], (∇) Payard and Coutanceau [5], and (+) Pruppacher et al. [11].

may be noted. The first appearance of separation occurred above a Reynolds number of 20. The computed variations of the wake length and angle of separation with Reynolds number are presented in Figs. 5 and 6, respectively. Also shown are the wake lengths and angles of separation observed in the experiments performed by Taneda [10], Payard and Coutanceau [5], Pruppacher et al. [11], and Nakamura [6]. The agreement shown in Figs. 5 and 6 between the computed variations and the experimental observations is very good.

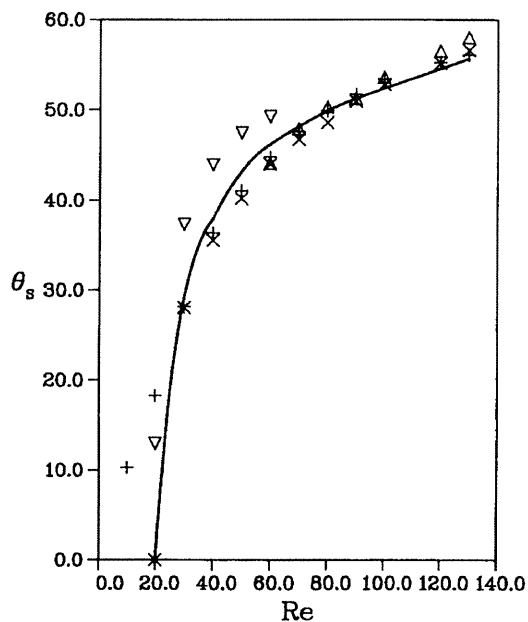


Fig. 6 Variation of the flow separation angle, θ , (degrees), with Reynolds number for the sphere. The present results (solid curve) are compared with the experimental data of (Δ) Taneda [10], (∇) Payard and Coutanceau [5], (\times) Nakamura [6], and (+) Pruppacher et al. [11].

The dimensionless drag coefficient C_D is defined as

$$C_D = \frac{F}{\pi \rho U_\infty^2 a^2} \quad (14)$$

where F is the total drag force on the sphere and a is the sphere radius. The equations for the friction drag and the pressure drag are

$$F_f = -2\pi a^2 \int_0^\pi \left(\frac{1}{h_2} \frac{\partial u_1}{\partial y_2} \right)_s \sin^2 \theta \, d\theta \quad (15)$$

and

$$F_p = -2\pi a^2 \int_0^\pi p \cos \theta \sin \theta \, d\theta \quad (16)$$

respectively. The drag forces on the sphere's surface were calculated by assuming that the pressure on the surface was equal to the pressure in the computational cell directly above the surface and that the variation of the tangential velocity was linear between the surface and the first u_1 velocity node. With the surface pressure and the normal gradient of the tangential velocity thereby determined, the drag forces F_f and F_p were then computed from Eqs. (15) and (16) using the trapezoidal rule. The predicted variation of the drag coefficient with Reynolds number is plotted in Fig. 7, along with the experimental data of Pruppacher and Steinberger [12] and Beard and Pruppacher [13]. The present results for the drag coefficient are seen to be in very good agreement with their experimental observations.

The advantage of using the coordinate transformation in the above calculations

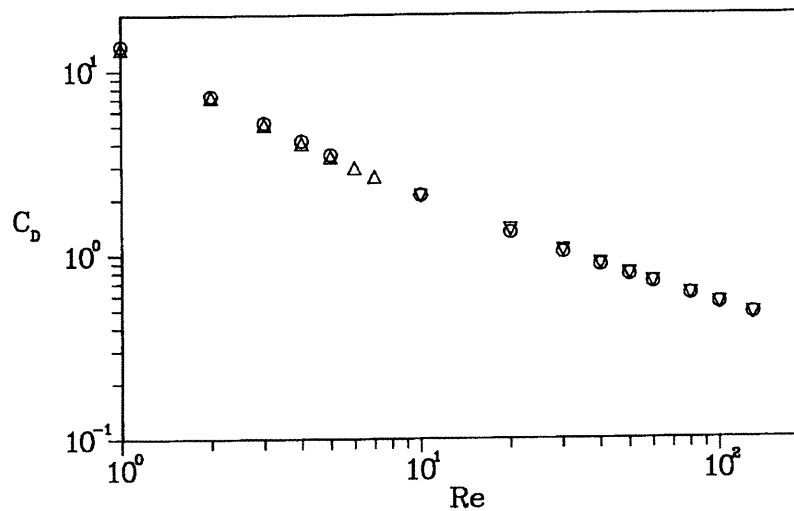


Fig. 7 Variation of drag coefficient C_D with Reynolds number for the sphere. (○) Present results and experimental data of (Δ) Pruppacher and Steinberger [12] and (▽) Beard and Pruppacher [13].

should be discussed. Every boundary of the flow domain coincided exactly with only one of the transformed coordinates, i.e., a stream function or velocity potential coordinate. This characteristic greatly simplified specification of the boundary conditions and will be especially useful in subsequent sections when mass transfer and internal circulation are considered for the sphere. Investigation of flow fields with complicated velocity or scalar boundary conditions would be impractical using a numerical method that requires considerable interpolation of boundary values. Overcoming this obstacle was the objective in adapting the numerical solution procedure of Patankar [1] to orthogonal curvilinear coordinates.

As an additional validation of the numerical method we predicted the flow past a circular cylinder, including its wake length, flow separation angle, and drag coefficient for Reynolds numbers between 1 and 40. We present a comparison between our predicted wake lengths and those measured by Taneda [14] and Coutanceau and Bouard [15] in Fig. 8. For a description of the predicted cylinder flow the reader may consult reference [9].

Mass Transfer from a Solid Sphere

The mass transport model presented in Eq. (7) was used to simulate diffusional mass flux from the sphere's surface. It is convenient to define a general dependent variable as the dimensionless mass fraction m^* , with

$$m^* = \frac{m_i - m_{i,\infty}}{m_{i,s} - m_{i,\infty}} \quad (17)$$

where $m_{i,\infty}$ is set to zero and the rate of mass efflux from the sphere's surface is adjusted by varying the boundary mass fraction $m_{i,s}$.

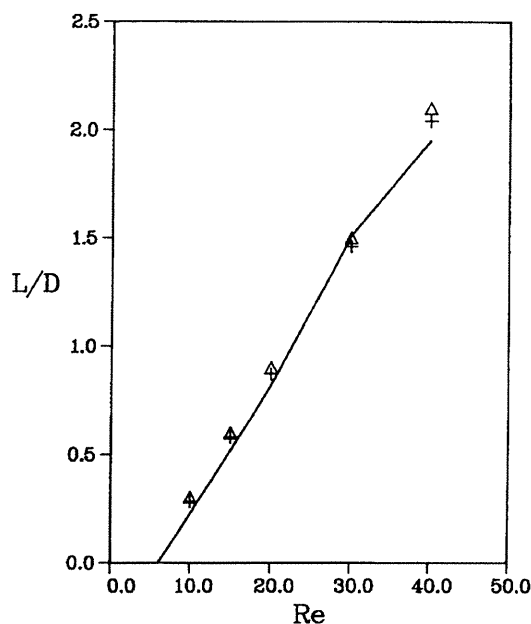


Fig. 8 Variation of wake length with Reynolds number for a circular cylinder. The present results (solid curve) are compared with the experimental data of (Δ) Taneda [14] and (+) Coutanceau and Bouard [15].

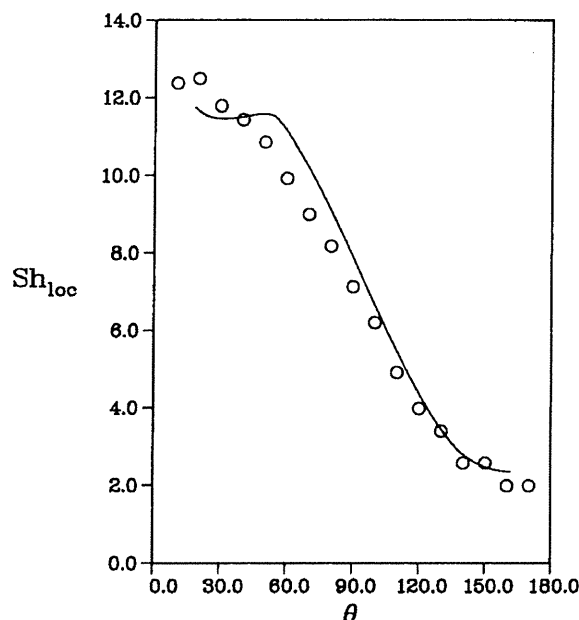


Fig. 9 Variation of the local Sherwood number Sh_{loc} over the surface of the sphere; $Re = 48$, $Sc = 2.5$, and $m_{i,s} = 2.816 \times 10^{-4}$. The present results (solid curve) are compared with the experimental data of Frössling [16] (○).

For very low values of $m_{i,s}$ the diffusional mass flux will be correspondingly small and the fluid motion will not be altered appreciably. Under these conditions the results obtained from other numerical solutions, where the diffusional mass flux was solved for independent of the velocity field, should agree with the results obtained by the present method. As $m_{i,s}$ is increased, the normal velocity at the sphere's surface will likewise increase according to Eq. (7).

Computations were performed to validate the model for low rates of mass transfer. The only experimental data available in the literature reporting local rates of mass transfer from a sphere in this Reynolds number regime are those of Frössling, cited in [3]. Frössling [16] measured photographically the local change in radius of naphthalene spheres suspended in a uniform air stream. Two of the Reynolds numbers he considered (48 and 136) were low enough to be simulated with an axisymmetric flow model. The mass fraction of the naphthalene vapor at the sphere's surface in Frössling's experiments was calculated from available correlations of its vapor pressure to be 2.816×10^{-4} . The Schmidt number for naphthalene vapor in air, given in [3], is 2.5. The effects of spatial gradients of the fluid density and diffusivity were assumed to be negligible for these calculations.

The results of a calculation performed to simulate one of Frössling's experiments are shown in Fig. 9, where the local and average Sherwood numbers are defined by

$$Sh_{loc} = - \frac{2}{h_2} \frac{\partial m^*}{\partial y_2} \bigg|_s \quad (18)$$

LAMINAR FLOW PAST A SPHERE

69

and

$$\text{Sh} = \frac{1}{2} \int_0^\pi \text{Sh}_{\text{loc}} \sin \theta \, d\theta \quad (19)$$

respectively. The predicted variation of the local Sherwood number over the sphere's surface departs from Frössling's observations only near the stagnation points. Numerical integration of the computed local Sherwood number and Frössling's data was performed using Eq. (19) and the trapezoidal rule. Comparison of the average Sherwood numbers obtained produced differences of 4 and 8% for Reynolds numbers of 48 and 136, respectively. The agreement of the present results with Frössling's observations was considered good enough to proceed.

Further calculations were performed to compare results of the present method with the results of past numerical work for low rates of mass transfer. Clift et al. [3] presented the following correlation of the available numerical solutions for Reynolds numbers between 1 and 400 and Schmidt numbers between 0.25 and 100 to within 3%:

$$\frac{\text{Sh} - 1}{\text{Sc}^{1/3}} = \left(1 + \frac{1}{\text{ReSc}} \right)^{1/3} \text{Re}^{0.41} \quad (20)$$

For the remaining calculations, three Reynolds numbers were considered: 10, 20, and 100. The Schmidt number was set to 1.0, a value appropriate for many gaseous fuel-air systems. For comparison with the above correlation, which is for low mass transfer rates, the surface mass fraction was set to 10^{-6} . The results, listed in Table 1, show agreement with the above correlation to within 4%. Contours of the dimensionless mass fraction m^* are plotted in Fig. 10 for a Reynolds number of 100.

To study the effects of high rates of mass transfer on the average Sherwood number and on the different drag coefficients, C_f and C_p , the mass fraction at the sphere's surface was raised from 10^{-6} to 0.7 for Reynolds numbers of 20 and 100 and to 0.5 for a Reynolds number of 10.

The effect on the flow streamlines induced by a high surface mass fraction is shown in Fig. 11 for a Reynolds number of 100. The downstream wake circulation has increased considerably for this Reynolds number. These streamlines should be compared with those shown in Fig. 4 for the case of no mass transfer.

In Fig. 12 contours of the dimensionless mass fraction m^* are drawn for

Table 1 Comparison of Numerically Predicted Sherwood Numbers, Sh , for Low Rates of Mass Transfer from a Sphere, $\text{Sc} = 1.0$

Re	Present results	Eq. (20)
10	3.535	3.653
20	4.305	4.471
100	7.562	7.629

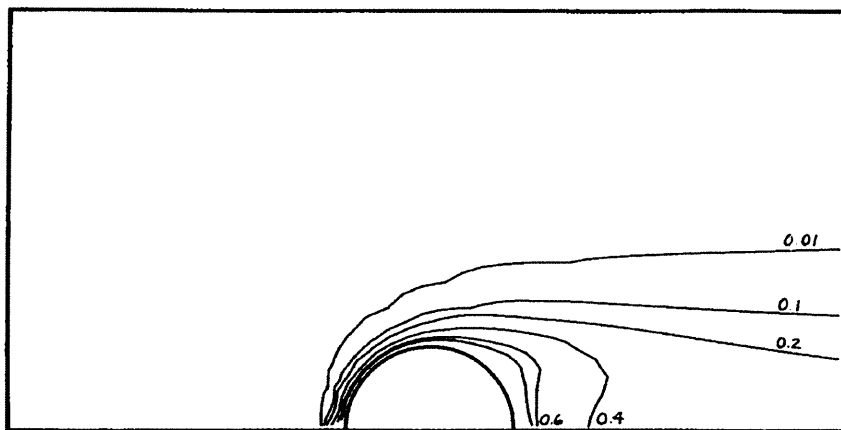


Fig. 10 Contours of the dimensionless mass fraction coefficient m^* for flow past a sphere with $m_{i,s} = 10^{-6}$, $Sc = 1.0$, and a Reynolds number of 100.

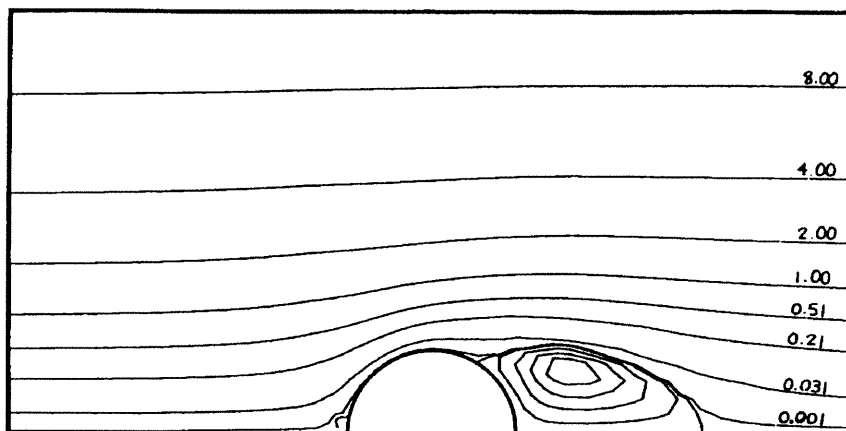


Fig. 11 Streamlines for flow past a sphere experiencing large radial mass efflux; $Re = 100$, $Sc = 1.0$, and $m_{i,s} = 0.5$. Values of the dimensionless stream function Ψ are shown for selected contours. Values of Ψ for the recirculating wake region are given as follows, starting from the center: $\Psi = -0.04, -0.03, -0.02, -0.01, -0.0021$.

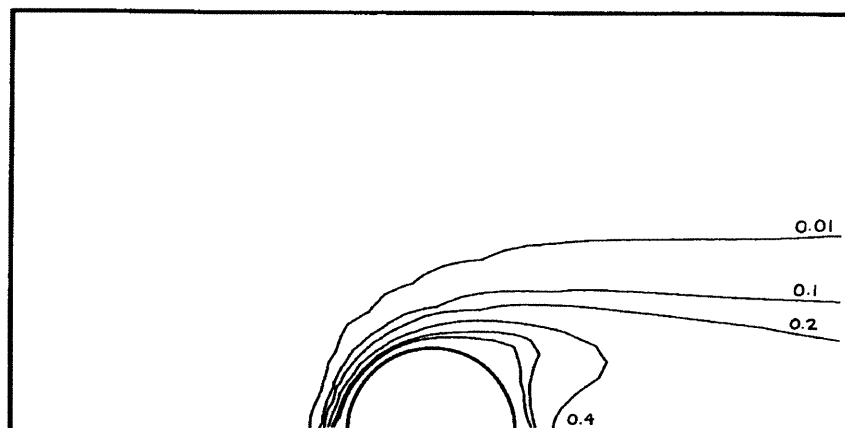


Fig. 12 Contours of the dimensionless mass fraction m^* for flow past a sphere experiencing large radial mass efflux; $Re = 100$, $Sc = 1.0$, $m_{i,s} = 0.5$.

LAMINAR FLOW PAST A SPHERE

71

$m_{i,s} = 0.5$. Comparison with Fig. 10 shows a reduction in gradient of m^* normal to the sphere's surface. The maximum predicted average Sherwood number [Eq. (19)] occurred for the lowest value of surface mass fraction. Normalizing the predicted Sherwood numbers for higher rates of mass transfer by these maximum values shows a linear correlation between the surface mass fraction and the normalized Sherwood number for Reynolds numbers of 10, 20, and 100. This is illustrated in Fig. 13. The line shown is a least-squares fit of the values computed for a Reynolds number of 20.

The effect of large radial mass efflux on the sphere's overall drag is shown in Fig. 14. The mass transfer appreciably reduces the overall drag, so the drag coefficients were normalized to the values computed for no mass transfer. This reduction in drag is created by a decreased tangential velocity gradient at the sphere's surface, while the pressure distribution over the surface remains largely unchanged. In Fig. 15 this effect is illustrated for a Reynolds number of 100 by plotting the friction and pressure drag coefficients and their sum against the surface mass fraction. While the friction drag is reduced considerably, the pressure drag is only slightly increased by an increasing rate of mass transfer.

The reduction in Sherwood number [Eq. (18)] with increasing rate of surface mass transfer is due to the fact that blowing at the sphere's surface reduces the mass fraction gradient there. The reduction of the friction drag has also been noted by Hamielec et al. [7] for a sphere with an imposed nonuniform normal surface velocity. Their numerical results independently confirm the trends noted in Figs. 14 and 15.

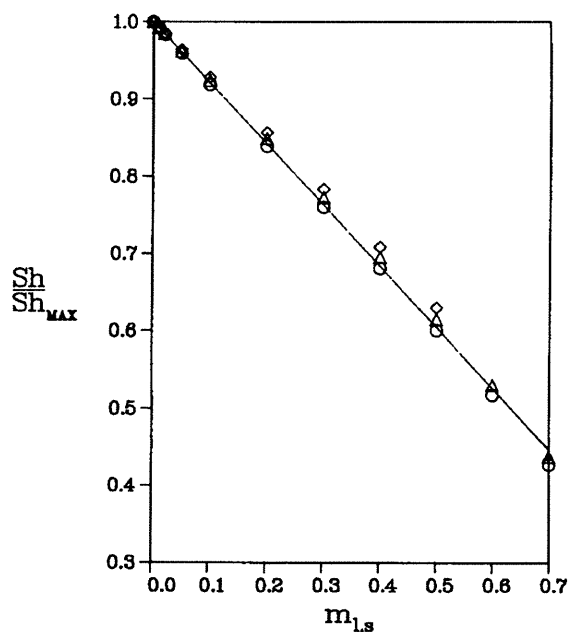


Fig. 13 Variation of the average Sherwood number Sh (normalized by the maximum attained for $m_{i,s} = 10^{-6}$) with surface mass fraction $m_{i,s}$ for the sphere; $Sc = 1.0$. Results are plotted for Reynolds numbers of (\diamond) 10, (\triangle) 20, and (\circ) 100.

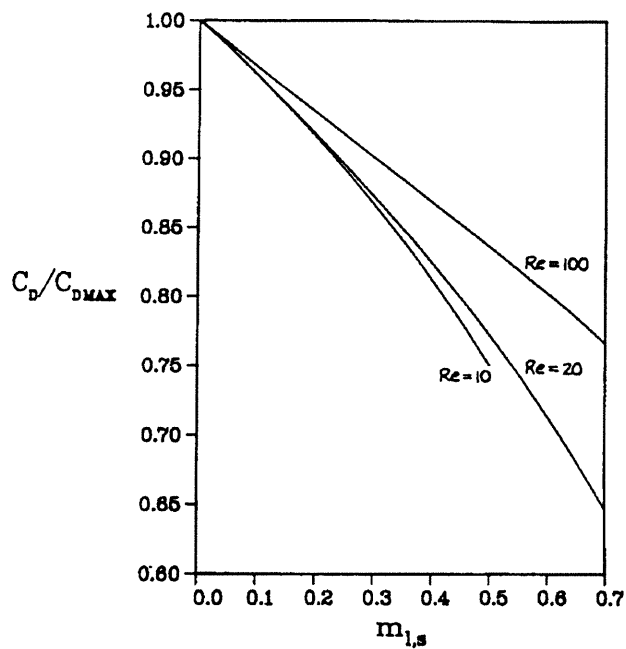


Fig. 14 Variation of the drag coefficient C_D (normalized by the maximum attained for $m_{l,s} = 10^{-6}$) with surface mass fraction $m_{l,s}$ for the sphere; $Sc = 1.0$.

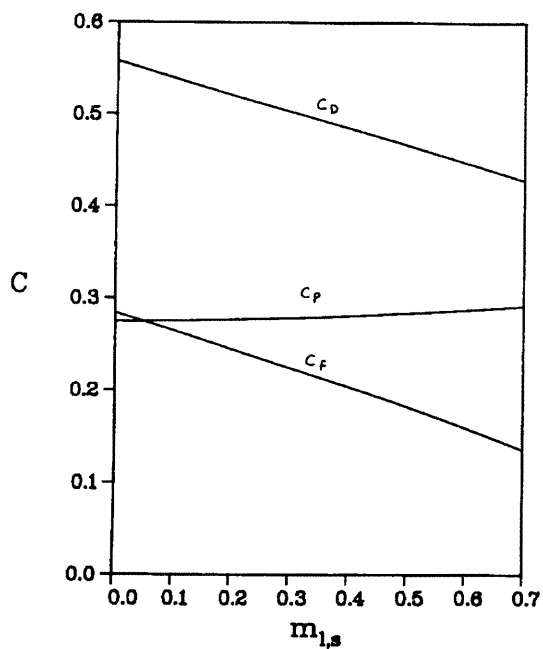


Fig. 15 Variation of the drag coefficients with surface mass fraction $m_{l,s}$ for the sphere; $Sc = 1.0$, $Re = 100$.

LAMINAR FLOW PAST A SPHERE

73

Mass Transfer from a Liquid Sphere

Predictions for the case of low mass transfer rate from a sphere with internal circulation were made for a Reynolds number of 100. This was accomplished by prescribing the tangential surface velocity, $u_{1,s}$, distributions at the sphere's surface according to Rivkind et al. [2]. The velocity distributions in [2] were computed as a function of the internal-to-external viscosity ratio μ^* of the fluids. Three ratios were considered in performing the computations for a Reynolds number of 100. These were 0, 1, and 10, where a ratio of infinity corresponds to a solid sphere and a ratio of 0 corresponds to a gaseous sphere.

The surface velocity distributions used with the present method are shown in Fig. 16. An important feature of the flow over a liquid sphere is that reducing the viscosity ratio increases the mobility of the boundary. This in turn reduces the tangential velocity gradient normal to the surface and therefore the friction drag. Separation of the flow from the sphere's surface is delayed until, for a viscosity ratio of about 1, the flow does not separate and there is no recirculating wake behind the sphere.

Values of the predicted drag coefficients C_f and C_p for the three viscosity ratios considered here are listed in Table 2, along with the values previously computed for a solid sphere. The drag for a gaseous sphere is entirely due to pressure drag concentrated at the stagnation points. The slight deviation of the pressure distribution in this case from the symmetric distribution of potential flow is difficult to determine accurately using the present method and the values presented in [2]. The close agreement (not shown here) between our predicted flow streamlines and those presented

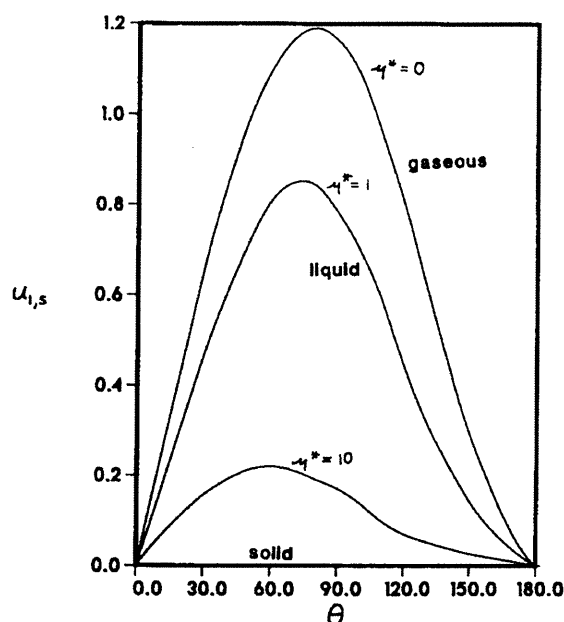


Fig. 16 Tangential surface velocity $u_{1,s}$ profiles used in the calculations for flow past a sphere, $Re = 100$, for three different internal-to-external viscosity ratios μ^* . From Rivkind et al. [2].

Table 2 Predicted Values of the Flow Field Characteristics for a Liquid Sphere, $Re = 100$ and $Sc = 1.0$; Values of the Drag Coefficient C_D Predicted by Rivkind et al. [2]

μ^*	C_f	C_p	C_D	C_D [2]	Sh
0.0	0.000	0.095	0.095	0.200	10.761
1.0	0.188	0.155	0.343	0.370	9.778
10.0	0.268	0.250	0.518		8.071
∞	0.284	0.274	0.558	0.555	7.562

in [4] indicated that the present results differ from the results of [2] only near the stagnation points.

For each of the three cases discussed above the surface mass fraction was set to 10^{-6} . Increasing the mobility of the surface significantly increased the mass fraction gradient normal to the surface. The results for the average Sherwood number, listed in Table 2, confirm this.

Higher rates of mass transfer from a liquid sphere with internal circulation were not computed because of the strong coupling that must exist between the normal and tangential velocity components at the sphere's surface. However, the increase noted in the average Sherwood number for lower rates of mass transfer from a sphere with internal circulation would likely offset the reduction predicted above in the case of higher rates of mass transfer from a solid sphere. The modeling of both effects would require solving for the internal flow field with careful consideration of the interfacial boundary conditions. The present method for solution of the external flow field would be useful in this case as the interfacial boundary coincides with only one transformed coordinate.

CONCLUSIONS

The equations governing laminar flow past a sphere with surface mass transfer have been solved using a modified version of the numerical method of Patankar [1]. The method was originally developed [1] in Cartesian and cylindrical coordinates and was extended in this work for the solution of two-dimensional flow fields in orthogonal curvilinear coordinates. The coordinate system chosen in this work consisted of the streamlines and equipotential lines for potential flow past the sphere. With this coordinate system the boundaries of the computational mesh coincided exactly with the boundaries of the flow field. Mass transfer from the sphere's surface and the effect of internal circulation through boundary mobility were thereby also studied.

The Reynolds number range considered for flow past a sphere was between 1 and 130. The predicted variations of the wake length, angle of separation, and drag coefficient with Reynolds number were in good agreement with published experimental data.

Mass transfer from the sphere's surface was modeled by assuming that the molecular weight of the evaporating species is equal to the molecular weight of the free-stream species so that variations in density across the flow field could be neglected. The normal velocity distribution over the surface was determined from the normal gradient of mass fraction. The magnitude of the normal velocity was then

LAMINAR FLOW PAST A SPHERE

75

varied by changing the value of the surface mass fraction. The effects of high rates of mass transfer on the flow field were then investigated using the above approach for a Schmidt number of 1 and Reynolds numbers of 10, 20, and 100. The blowing effect of the surface mass efflux decreases the gradients of mass fraction and tangential velocity near the surface of the sphere. Thus, as the surface mass fraction increases, the drag coefficient is reduced, with greater effects noted for lower Reynolds numbers. The computed average Sherwood number decreases linearly with increasing surface mass fraction.

The effect of internal circulation on the flow field surrounding a liquid sphere was investigated for a Reynolds number of 100. The internal circulation of the sphere was modeled using tangential surface velocity distributions computed by Rivkind et al. [2]. The velocity distributions used were for droplet-to-free-stream viscosity ratios of 0, 1, and 10. The reduction in the drag coefficient with increased boundary mobility was noted, as it was in [2]. A substantial increase in the mass fraction gradient with increased boundary mobility was predicted. The average Sherwood number was thereby increased.

APPENDIX

Orthogonal Curvilinear Coordinates

Here we follow closely the formulas presented by Sedov [17]. Let y_i and x_i denote the coordinates of points in the Euclidean coordinate systems K and K' , respectively, and let

$$y_i = y_i(x_1, x_2, x_3) \quad (i = 1, 2, 3) \quad (A1)$$

a given function of x_i . Equation (A1) can be solved for x_i in the neighborhood of an arbitrary point in the regions K and K' and can be put in the form

$$x_i = x_i(y_1, y_2, y_3) \quad (i = 1, 2, 3) \quad (A2)$$

From differential calculus, we have

$$dx_i = \frac{\partial x_i}{\partial y_\alpha} dy_\alpha \quad (A3a)$$

and

$$dy_i = \frac{\partial y_i}{\partial x_\alpha} dx_\alpha \quad (A3b)$$

Let \mathbf{e}_i and \mathbf{e}'_i be the unit reference vectors in the coordinate systems K and K' , respectively. For an arbitrary differential displacement vector $d\mathbf{s}$, the following holds:

$$d\mathbf{s} = dx_1 d\mathbf{e}'_1 + dx_2 d\mathbf{e}'_2 + dx_3 d\mathbf{e}'_3 = dy_1 d\mathbf{e}_1 + dy_2 d\mathbf{e}_2 + dy_3 d\mathbf{e}_3 \quad (A4)$$

The formulas relating \mathbf{e}'_i and \mathbf{e}_i are derived by substituting Eq. (A3) into Eq. (A4), giving

$$dy_\alpha \mathbf{e}_\alpha = \frac{\partial x_\beta}{\partial y_\alpha} dy_\alpha \mathbf{e}'_\beta \quad (A5a)$$

and

$$dx_\alpha e'_\alpha = \frac{\partial y_\beta}{\partial x_\alpha} dx_\alpha e_\beta \quad (\text{A5b})$$

Simplifying Eq. (A5), we obtain

$$e_\alpha = \frac{\partial x_\beta}{\partial y_\alpha} e'_\beta \quad (\text{A6a})$$

and

$$e'_\alpha = \frac{\partial y_\beta}{\partial x_\alpha} e_\beta \quad (\text{A6b})$$

Equation (A6) then defines the matrix of the transformation \mathbf{A} as

$$\mathbf{A} \equiv \left[\frac{\partial x^i}{\partial y^k} \right] = \begin{bmatrix} \frac{\partial x^1}{\partial y^1} & \frac{\partial x^1}{\partial y^2} & \frac{\partial x^1}{\partial y^3} \\ \frac{\partial x^2}{\partial y^1} & \frac{\partial x^2}{\partial y^2} & \frac{\partial x^2}{\partial y^3} \\ \frac{\partial x^3}{\partial y^1} & \frac{\partial x^3}{\partial y^2} & \frac{\partial x^3}{\partial y^3} \end{bmatrix} \quad (\text{A7a})$$

with its inverse matrix \mathbf{A}^{-1} defined as

$$\mathbf{A}^{-1} \equiv \left[\frac{\partial y^i}{\partial x^k} \right] \quad (\text{A7b})$$

where i denotes the matrix row and k the column. Equation (A6) can now be written in matrix form as

$$\{e_\alpha\} = \{e'_\beta\} \mathbf{A} \quad (\text{A8a})$$

and

$$\{e'_\alpha\} = \{e_\beta\} \mathbf{A}^{-1} \quad (\text{A8b})$$

where $\{ \}$ denotes a row matrix.

In Euclidean space a differential arc length ds is defined, using Eq. (A4), as

$$ds^2 \equiv ds \cdot ds = g'_{\alpha\beta} dx_\alpha dx_\beta \quad (\text{A9})$$

where $g'_{\alpha\beta}$ is the Euclidean metric tensor for coordinate system K' . The formula for transforming $g'_{\alpha\beta}$ to the new coordinate system, K , may be shown to be

LAMINAR FLOW PAST A SPHERE

77

$$g_{ik} = \frac{\partial x^\alpha}{\partial y^i} \frac{\partial x^\beta}{\partial y^k} g'_{\alpha\beta} \quad (\text{A10})$$

If K' is a Cartesian coordinate system, then

$$g'_{\alpha\beta} = \delta_{\alpha\beta} \begin{cases} = 1 & \alpha = \beta \\ = 0 & \alpha \neq \beta \end{cases} \quad (\text{A11})$$

and g_{ik} is seen to be a function only of the coefficients of the matrix A . If the new coordinate system K is chosen to be orthogonal, the off-diagonal terms of g_{ik} will be zero and a scale factor h_i may be defined, using

$$g_{ik} = \begin{cases} = h_i^2 & i = k \\ = 0 & i \neq k \end{cases} \quad (\text{A12})$$

as

$$h_i \equiv \left\{ \left(\frac{\partial x_1}{\partial y_i} \right)^2 + \left(\frac{\partial x_2}{\partial y_i} \right)^2 + \left(\frac{\partial x_3}{\partial y_i} \right)^2 \right\}^{1/2} \quad (\text{A13})$$

For orthogonal coordinate systems the differential arc length ds , defined in Eq. (A9), then reduces to

$$ds = h_i dy_i \quad (\text{A14})$$

Similarly, differential areas dA_{ij} and volume dV may be derived from Eq. (A14) for orthogonal coordinate systems as

$$dA_{ij} = h_i h_j dy_i dy_j \quad (\text{no summation, } i \neq j) \quad (\text{A15})$$

and

$$dV = h_1 h_2 h_3 dy_1 dy_2 dy_3 \quad (\text{A16})$$

respectively.

In the following section the coordinate transformations chosen for the sphere will be presented along with the computational procedures used to obtain the values of the scale factors h_i over the flow domain.

Coordinate Transformation Used for the Sphere

The potential flow solution for the sphere may be expressed using geometry similar to that shown in Fig. 1 if we recognize that x_1 and x_2 are the familiar z - r coordinates of cylindrical geometry. Here we assume axisymmetric flow, and though we need not consider variations in the azimuthal direction x_3 , h_3 will remain the

same as in cylindrical coordinates, equal to x_2 . In terms of polar coordinates r and θ , the velocity potential ϕ and the Stokes stream function ψ are then

$$\phi = U_{\infty} \left(r + \frac{1}{2} \frac{a^3}{r^2} \right) \cos \theta \quad (\text{A17})$$

and

$$\psi = \frac{1}{2} U_{\infty} \left(r^2 - \frac{a^3}{r} \right) \sin^2 \theta \quad (\text{A18})$$

respectively, where U_{∞} is the free-stream velocity, a is the radius of the sphere, and

$$r = x_1^2 + x_2^2 \quad (\text{A19})$$

and

$$\theta = \tan^{-1} \left(\frac{x_2}{x_1} \right) \quad (\text{A20})$$

We now normalize the velocity potential and Stokes stream function by $U_{\infty}a$ and $U_{\infty}a^2$, respectively, and let $R = r/a$, to obtain the dimensionless expressions for the transformed coordinates y_1 and y_2 :

$$y_1 = \frac{\phi}{U_{\infty}a} = \frac{1}{2} \left(2R + \frac{1}{R^2} \right) \cos \theta \quad (\text{A21})$$

and

$$y_2 = \frac{\psi}{U_{\infty}a^2} = \frac{1}{2} \left(R^2 - \frac{1}{R} \right) \sin^2 \theta \quad (\text{A22})$$

respectively.

In order to obtain the scale factors h_1 and h_2 for an arbitrary point (y_1, y_2) , relations (A21) and (A22) must be inverted to obtain R and θ , and thus also x_1 and x_2 , in terms of y_1 and y_2 . The partial derivatives that appear as coefficients in the inverse transformation matrix \mathbf{A}^{-1} , Eq. (A7b), are then derived from Eqs. (A21) and (A22). Once the coefficients of the matrix \mathbf{A}^{-1} are assembled, \mathbf{A}^{-1} is inverted to obtain the coefficients of the matrix of the transformation, \mathbf{A} . The scale factors h_1 and h_2 are then derived from the coefficients of \mathbf{A} .

To begin, we eliminate θ from Eqs. (A21) and (A22) by using the trigonometric relation

$$\sin^2 \theta + \cos^2 \theta = 1 \quad (\text{A23})$$

Substituting Eqs. (A21) and (A22) for $\sin \theta$ and $\cos \theta$ in Eq. (A23) gives, with some rearranging,

LAMINAR FLOW PAST A SPHERE

79

$$R^9 - (y_1^2 + 2y_2^2)R^7 + (y_1^2 - 2y_2^2)R^4 - \frac{3}{4}R^3 - \frac{1}{2}y_2R - \frac{1}{4} = 0 \quad (A24)$$

a ninth-order polynomial in R . For a given (y_1, y_2) coordinate, Eq. (A24) may be solved for R numerically by Newton's method. θ then follows from the relation

$$\theta = \tan^{-1} \left\{ \frac{[y_2/(2R - 2/R)]^{1/2}}{y_1/(2R - 1/R^2)} \right\} \quad (A25)$$

and (x_1, x_2) from

$$x_1 = Ra \cos \theta \quad (A26)$$

and

$$x_2 = Ra \sin \theta \quad (A27)$$

Using Eqs. (A21), (A22), (A26), (A27), and (A19), y_1 and y_2 may be expressed as functions of x_1 and x_2 , giving

$$y_1 = \frac{x_1}{a} + \frac{1}{2} a^2 x_1 (x_1^2 + x_2^2)^{-3/2} \quad (A28)$$

and

$$y_2 = \frac{1}{2} \left[\frac{x_2^2}{a^2} - \frac{ax_2^2}{(x_1^2 + x_2^2)^{3/2}} \right] \quad (A29)$$

The partial derivatives that appear as coefficients in the matrix \mathbf{A}^{-1} may now be derived for the sphere. Having performed the differentiations in Eq. (A7b), the following relations were noted:

$$\frac{\partial y_1}{\partial x_1} = \frac{1}{x_2} \frac{\partial y_2}{\partial x_2} \quad (A30)$$

and

$$\frac{\partial y_1}{\partial x_2} = -\frac{1}{x_2} \frac{\partial y_2}{\partial x_1} \quad (A31)$$

Therefore, only two of the coefficients of \mathbf{A}^{-1} are independent and need be presented. These are

$$\frac{\partial y_1}{\partial x_1} = \frac{1}{a} + \frac{1}{2} a^2 \left[\frac{(x_1^2 + x_2^2)^{3/2} - 3x_1^2(x_1^2 + x_2^2)^{1/2}}{(x_1^2 + x_2^2)^3} \right] \quad (A32)$$

and

$$\frac{\partial y_1}{\partial x_2} = \frac{-3ax_1^2x_2^2}{2(x_1^2 + x_2^2)^{5/2}} \quad (\text{A33})$$

Now let

$$c = \frac{\partial y_1}{\partial x_1} \quad (\text{A34})$$

and

$$d = \frac{\partial y_1}{\partial x_2} \quad (\text{A35})$$

Substituting these expressions into Eq. (A7b) and using Eqs. (A30) and (A31), we have

$$\mathbf{A}^{-1} = \begin{bmatrix} c & d \\ -x_2d & x_2c \end{bmatrix} \quad (\text{A36})$$

Inverting Eq. (A36), we obtain the matrix of the transformation \mathbf{A} as

$$\mathbf{A} = \frac{1}{x_2(c^2 + d^2)} \begin{bmatrix} x_2c & -d \\ x_2d & c \end{bmatrix} \quad (\text{A37})$$

where, from Eq. (A7a), we see that

$$\frac{\partial x_1}{\partial y_1} = x_2 \frac{\partial x_2}{\partial y_2} = \frac{c}{c^2 + d^2} \quad (\text{A38})$$

and

$$\frac{\partial x_1}{\partial y_2} = -\frac{1}{x_2} \frac{\partial x_2}{\partial y_1} = \frac{-d}{x_2(c^2 + d^2)} \quad (\text{A39})$$

Finally, substituting Eqs. (A38) and (A39) into Eq. (A13), we have

$$h_1 = (c^2 + d^2)^{-1/2} \quad (\text{A40})$$

and

$$h_2 = \frac{1}{x_2} h_1 \quad (\text{A41})$$

LAMINAR FLOW PAST A SPHERE

81

and recall that

$$h_3 = x_2 \quad (\text{A42})$$

To reiterate, the procedure for determining the values of the scale factors h_i in the transformed plane is first to compute for a given (y_1, y_2) coordinate the corresponding Cartesian coordinate (x_1, x_2) , using Eqs. (A21)–(A27), and then for this Cartesian coordinate (x_1, x_2) to compute the scale factors h_i , using Eqs. (A32)–(A35) and, finally, Eqs. (A40)–(A42).

REFERENCES

1. S. V. Patankar, *Numerical Heat Transfer and Fluid Flow*, Hemisphere, Washington, D.C., 1980.
2. V. Ya. Rivkind, G. M. Ryskin, and G. A. Fishbein, Flow Around a Spherical Drop at Intermediate Reynolds Numbers, *Appl. Math. Mech.*, vol. 40, no. 4, pp. 741–745, 1976.
3. R. Clift, J. R. Grace, and M. E. Weber, *Bubbles, Drops, and Particles*, Academic Press, New York, 1978.
4. V. Ya. Rivkind and G. M. Ryskin, Flow Structure in Motion of a Spherical Drop in a Fluid Medium at Intermediate Reynolds Numbers, *Fluid Dyn. (USSR)*, vol. 11, pp. 5–12, 1976.
5. M. Payard and M. Coutanceau, Mécanique des Fluides, *C. R. Acad. Sci. Ser. B*, vol. 278, pp. 369–372, 1974.
6. I. Nakamura, Steady Wake Behind a Sphere, *Phys. Fluids*, vol. 19, no. 1, pp. 5–8, 1976.
7. A. E. Hamielec, T. W. Hoffman, and L. L. Ross, Numerical Solution of the Navier-Stokes Equation for Flow past Spheres: Part 1. Viscous Flow Around Spheres with and without Radial Mass Efflux, *AIChE J.*, vol. 13, pp. 212–219, 1967.
8. R. S. Brodkey, *The Phenomena of Fluid Motions*, p. 46, Addison-Wesley, Reading, Mass., 1967.
9. J. M. Conner, Calculation of Mass and Momentum Transfer for Laminar Flow Around a Cylinder and a Sphere, M.S. thesis, University of California, Irvine, 1984.
10. S. Taneda, Experimental Investigation of the Wake Behind a Sphere at Low Reynolds Numbers, *J. Phy. Soc. Jpn.*, vol. 11, no. 10, pp. 1104–1108, 1956.
11. H. R. Pruppacher, B. P. Le Clair, and A. E. Hamielec, Some Relations Between Drag and Flow Pattern of Viscous Flow Past a Sphere and a Cylinder at Low and Intermediate Reynolds Numbers, *J. Fluid Mech.*, vol. 44, part 4, pp. 781–790, 1970.
12. H. R. Pruppacher and E. H. Steinberger, An Experimental Determination of the Drag on a Sphere at Low Reynolds Numbers, *J. Appl. Phys.*, vol. 39, no. 9, pp. 4129–4132, 1968.
13. K. V. Beard and H. R. Pruppacher, A Determination of the Terminal Velocity and Drag of Small Water Drops by Means of a Wind Tunnel, *J. Atmos. Sci.*, vol. 26, pp. 1066–1072, 1969.
14. S. Taneda, Experimental Investigation of the Wake Behind a Sphere at Low Reynolds Numbers, *J. Phy. Soc. Jpn.*, vol. 11, no. 10, pp. 1104–1108, 1956.
15. M. Coutanceau and R. Bouard, Experimental Determination of the Main Features of the Viscous Flow in the Wake of a Circular Cylinder in Uniform Translation. Part 1. Steady Flow, *J. Fluid Mech.*, vol. 79, part 2, pp. 231–256, 1977.

16. N. Frössling, *Gerlands Beitr. Geophys.*, vol. 52, pp. 170–216, 1938.
17. L. I. Sedov, *Introduction to the Mechanics of a Continuous Medium*, pp. 1–10, Addison-Wesley, Reading, Mass., 1965.

Received October 13, 1986

Accepted January 9, 1987

Requests for reprints should be sent to S. E. Elghobashi.

RESEARCH ARTICLE

Large Eddy Simulation of Air Escape through a Hospital Isolation Room Single Hinged Doorway—Validation by Using Tracer Gases and Simulated Smoke Videos

Pekka E. Saarinen^{1*}, Petri Kalliomäki¹, Julian W. Tang², Hannu Koskela¹

1 Finnish Institute of Occupational Health, Turku, Finland, **2** Leicester Royal Infirmary, University Hospitals Leicester, Leicester, United Kingdom

* pekka.saarinen@ttl.fi



OPEN ACCESS

Citation: Saarinen PE, Kalliomäki P, Tang JW, Koskela H (2015) Large Eddy Simulation of Air Escape through a Hospital Isolation Room Single Hinged Doorway—Validation by Using Tracer Gases and Simulated Smoke Videos. PLoS ONE 10(7): e0130667. doi:10.1371/journal.pone.0130667

Editor: Josué Sznitman, Technion—Israel Institute of Technology, ISRAEL

Received: December 17, 2014

Accepted: May 24, 2015

Published: July 7, 2015

Copyright: © 2015 Saarinen et al. This is an open access article distributed under the terms of the [Creative Commons Attribution License](https://creativecommons.org/licenses/by/4.0/), which permits unrestricted use, distribution, and reproduction in any medium, provided the original author and source are credited.

Data Availability Statement: All relevant data are within the paper and its Supporting Information files.

Funding: This work was supported by the Finnish Funding Agency for Technology and Innovation. The funders had no role in study design, data collection and analysis, decision to publish, or preparation of the manuscript.

Competing Interests: Please note that author Julian W. Tang is a PLOS ONE Academic Editor. This does not alter the authors' adherence to all the PLOS ONE policies on sharing data and materials. None of the

Abstract

The use of hospital isolation rooms has increased considerably in recent years due to the worldwide outbreaks of various emerging infectious diseases. However, the passage of staff through isolation room doors is suspected to be a cause of containment failure, especially in case of hinged doors. It is therefore important to minimize inadvertent contaminant airflow leakage across the doorway during such movements. To this end, it is essential to investigate the behavior of such airflows, especially the overall volume of air that can potentially leak across the doorway during door-opening and human passage. Experimental measurements using full-scale mock-ups are expensive and labour intensive. A useful alternative approach is the application of Computational Fluid Dynamics (CFD) modelling using a time-resolved Large Eddy Simulation (LES) method. In this study simulated air flow patterns are qualitatively compared with experimental ones, and the simulated total volume of air that escapes is compared with the experimentally measured volume. It is shown that the LES method is able to reproduce, at room scale, the complex transient airflows generated during door-opening/closing motions and the passage of a human figure through the doorway between two rooms. This was a basic test case that was performed in an isothermal environment without ventilation. However, the advantage of the CFD approach is that the addition of ventilation airflows and a temperature difference between the rooms is, in principle, a relatively simple task. A standard method to observe flow structures is dosing smoke into the flow. In this paper we introduce graphical methods to simulate smoke experiments by LES, making it very easy to compare the CFD simulation to the experiments. The results demonstrate that the transient CFD simulation is a promising tool to compare different isolation room scenarios without the need to construct full-scale experimental models. The CFD model is able to reproduce the complex airflows and estimate the volume of air escaping as a function of time. In this test, the calculated migrated air volume in the CFD model differed by 20% from the experimental tracer gas measurements. In the case containing only a hinged door operation, without passage, the difference was only 10%.

other coauthors have any competing interests to declare, regarding the publication of this manuscript.

Introduction

The usage of hospital isolation rooms has been increasing world-wide after the demonstration of the airborne transmission potential of various infectious agents, such as severe acute respiratory syndrome-associated coronavirus (SARS-CoV) [1–6] and influenza viruses [7–11]—though for human-to-human airborne transmission of influenza, there has been an ongoing, fierce debate about the proportion of transmission that is truly airborne [12–18]. Concerns about airborne transmission have even been raised for Ebola virus during the current epidemic in West Africa, even though this virus is normally transmitted via direct contact [19]. It is this heightened awareness of the potential for airborne transmission of various infectious agents, together with the traditionally precautionary approach to infection control that means that patients infected with potentially highly contagious diseases are now being routinely quarantined in negative pressure isolation rooms to prevent further spreading of the disease, to protect patients, staff and visitors.

However, despite these precautions, containment failures can happen and the operation of the isolation room doors could be one of the main contributors [20–22]. A case study by Tang et al. [20] showed that the operation of isolation room doors can lead to containment failure. In the present study, the air migration from the isolation room induced by door-opening and passage has been modelled. Even though the air volume migrated (AVM) is closely connected to the number of pathogens potentially escaping, a linear dependence requires that the pathogens are aerosolized and fully airborne, and therefore capable of long-range transmission. Whilst this is the case for some infectious agents, others are transmitted by larger droplets, subject to gravitational settling. A recent review by Fernstrom and Goldblatt [23] summarizes the research on the aerobiology of infectious aerosols. The division between airborne and droplet transmission is complicated by the fact that in dry air, the droplets desiccate rapidly, leaving so-called droplet nuclei that are airborne. This may happen prior to the droplet/droplet nuclei reaching the floor. Or the droplet nuclei can be resuspended and become airborne again after settling onto a surface. The evaporation of water-containing droplets is significantly reduced in air of high humidity, making them more prone to settling under gravity [24]. According to the definition adopted by WHO, particles with a diameter of less than 5 μm are considered airborne. However, under normal air conditions, particles up to 50 μm dry out completely within 0.5 seconds, and particles up to 100 μm would totally evaporate before falling 2 m [25]. So droplets/particles of these diameters to begin with may quickly evaporate to fall within this so-called ‘airborne’ range. A human cough contains both droplets and fine, airborne particles that can be simulated by tracer gas [24]. The infectious droplet nuclei generated from human respiratory sources have a diameter 0.5–5 μm with average being less than 1 μm [26, 27]. The estimations about the extent to which airborne transmission contributes to the overall infection rates in hospitals vary from 10% to 30% [23].

Hence, there is a need to understand the flow patterns caused by door motion and human (staff) passage through these isolation room doorways. In this paper we compare a Computational Fluid Dynamics (CFD) modelling approach using a time-resolved Large Eddy Simulation method (LES), to measurements obtained from a full-scale mock-up with identical geometry, to determine, whether CFD is an accurate and robust alternative method for understanding and characterising the flow behavior leading to possible containment failure. To this end we also introduce methods to produce CFD-simulated smoke videos that are easily comparable to those produced experimentally in the same experimental scenarios.

Most hospital isolation rooms use manually-operated or automatic hinged doors, though perhaps an increasing number are now using automatic sliding doors. Thus, for the experimental full-scale isolation room model both options were allowable, though the hinged door model

has been previously presented [28]. This paper combines a LES simulation with measurements from the full-scale experimental mock-up with the same geometry.

The test case was a simple isothermal scenario without ventilation, but including single hinged-door-opening and closing and a nurse passing through the doorway. Thus, the flow interactions arising from the moving door and human, alone, are presented, without any interference from any other sources. Addition of other factors such as ventilation, temperature differences between the rooms, or negative room pressure (i.e. unbalanced ventilation) would be a relatively simple next step. Flow structures near the doorway of the mock-up were examined and recorded in some detail by dosing smoke in one room and videoing its spread into the other room. Techniques were developed to construct similar simulated smoke videos from the LES results, enabling direct comparisons with the experimental videos. The ultimate purpose was to test the capability of time-resolved LES method to reproduce the full-scale air flows present in a real isolation room. The simulation was run on a standard workstation.

There are a few earlier studies reporting LES modelling of contaminant transport caused by door movement and passage through the doorway. Choi and Edwards [29] simulated a walking manikin going through an open doorway (i.e. in the absence of a door). In this study, they use their own immersed solid method [30] to model a walking human. They modelled several scenarios, varying the walking speed, initial position of the manikin, and initial distribution of the contaminant in the two rooms. The contaminant in their study consisted of particles, affected by gravity. The numerical methods used to solve the transport equations were also developed by the authors. In a later paper the same authors [31] simulated a more complex geometry, where a human is walking from a contaminated room to a clean room through a vestibule and two hinged or sliding doors. This simulation also includes ventilation (with an exhaust in the vestibule and small gaps below the doors), human plume, and several successive passages through the doors, with a gaseous contaminant. A clear advantage of the immersed solid methods is that they do not require re-meshing between the time steps, thereby allowing use of a large computational mesh. A study by Shih et al (case B in [32]), applied dynamic meshing to model the effect of opening and closing of a sliding door, without passage, on the spread of CO₂ contaminant from a human source inside a negative-pressure isolation room. Since dynamic meshing is computationally heavier than the immersed solid technique, the size of the mesh was less than 100 000 cells, though it was enough to model the CO₂ isosurfaces.

Measurements of cross-doorway airflow behavior by other researchers also exist, but with differing geometries, door-opening-closing cycles, and other experimental conditions, making comparisons difficult. However, based on extensive measurements in a water tank model and in a full-scale house, Kiel and Wilson [33] found an analytical formula giving the air volume migration (AVM) due to the combined effect of door-pumping and buoyancy. Their results were based on short door hold-opening times of the order of 1 s. In the isothermal case, without buoyancy, their formula reduces to $AVM = 2.3 \text{ m}^2 \text{ s } U_d$, where U_d is the velocity of the centre of the door. Tang et al. [22] have performed experiments by scaling down the present geometry to a water tank model, and using Reynolds number equivalent lengths and velocities. Smoke was then replaced by a food dye. They tested four different door constructions with results presented qualitatively using online videos. One of these scenarios can be compared to the present case.

When validating the simulations against the experimental measurements, the total AVM through the doorway was also compared. In the experiments, the air volume migrating from one room into the other was measured by tagging the air with tracer gases, and initially dosing different gases into different rooms at time zero (i.e. initial conditions). The amount of tracer escaping into the other room then gave the AVM.

Note that this study is a continuation of an earlier study simulating the door cycle without passage, see Saarinen et al. [34]. These CFD tests are a part of a larger research project [28, 35], containing measurements in the full-scale mock-up described above, in several different scenarios.

Methods

The Test Case

The mock-up actually consists of two rooms, the isolation room being connected to an ante-room by a hinged door in the middle of a separating wall (Fig 1). The smallest width of the doorway is 1.10 m and smallest height 2.06 m. The (inner) width and length of both the rooms is 4.7 m and 4.0 m, their heights being 3.0 m, giving a volume of 56.4 m³. The volume of the doorway gap, including the thickness of the frame, is 0.23 m³, of which 0.09 m³ is covered by the door. A manikin standing on a wheeled cart, moving along a rail, is used to represent a nurse walking through the doorway. The cart and the door are both computer-controlled.

The cycle with door operation and passage, used in the CFD simulation, is detailed in Fig 1. The direction of the nurse movement is from the isolation room to the anteroom. There are four movement phases, separated by waiting periods. The movements are (durations in parentheses, see also Fig 1):

- Nurse approaches the door (1.4 s followed by 2 s wait).
- The door opens 90 degrees (3 s followed by 0.5 s wait).
- Nurse moves through the doorway, into the anteroom (4.1 s, followed by 3.5 s wait).
- The door closes (5.4 s).

After these movements, the simulation was continued for ten seconds to monitor the fading air flows. This makes the total duration of the test case 30 s. The door door-opening time used (3 s) was near the minimum, since the door operator was at almost full speed. The hold-open time in the test case was rather long (8.1 s) to make sure that the manikin would not collide with the door in the laboratory experiments. However, doors equipped with a door-pump or an automatic door operator may have longer cycle times.

Both in the experiments and in the simulation, the steady travel speed of the nurse was 1 m/s, preceded and succeeded by an acceleration or deceleration ramp of 2 m/s². In contrast, the acceleration and deceleration of the door was so rapid that in the simulation it was opening and closing with constant angular velocity, without any ramps. The full opening angle of the door was 90 degrees.

Simulation Details

The simulation was performed with ANSYS CFX software using an incompressible, time-resolved large eddy simulation (LES) solver with a LES WALE subgrid model. The time step was chosen to be very short to ensure that the flow would normally travel no more than one mesh node spacing during one step, i.e., the maximal Courant number stayed below 1. The length of the time step was a constant 2 ms, until after 22.3 s of simulated time. Then after the door and nurse movements had ended, it was increased to 4 ms. The computational mesh was a pure tetra mesh comprising 11.7 million nodes (control volumes, corresponding to 68.7 million elements). In order to reduce the mesh size, a refined volume of approximately 6 m × (1–2.4) m × 2 m (greater width near the volume swept by the door), or some 20% of the overall volume of the rooms, was created in the path of the moving nurse and door. A dense mesh is

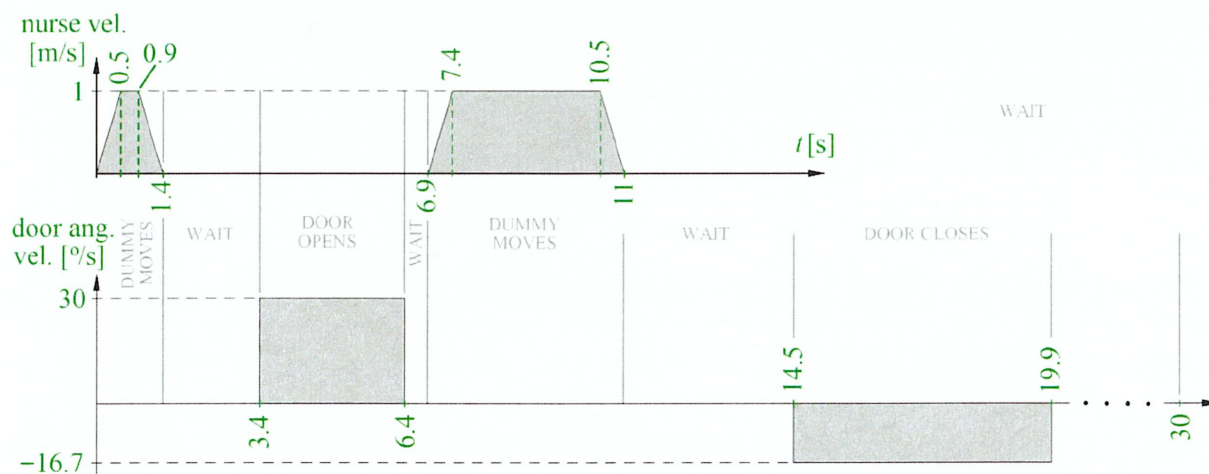
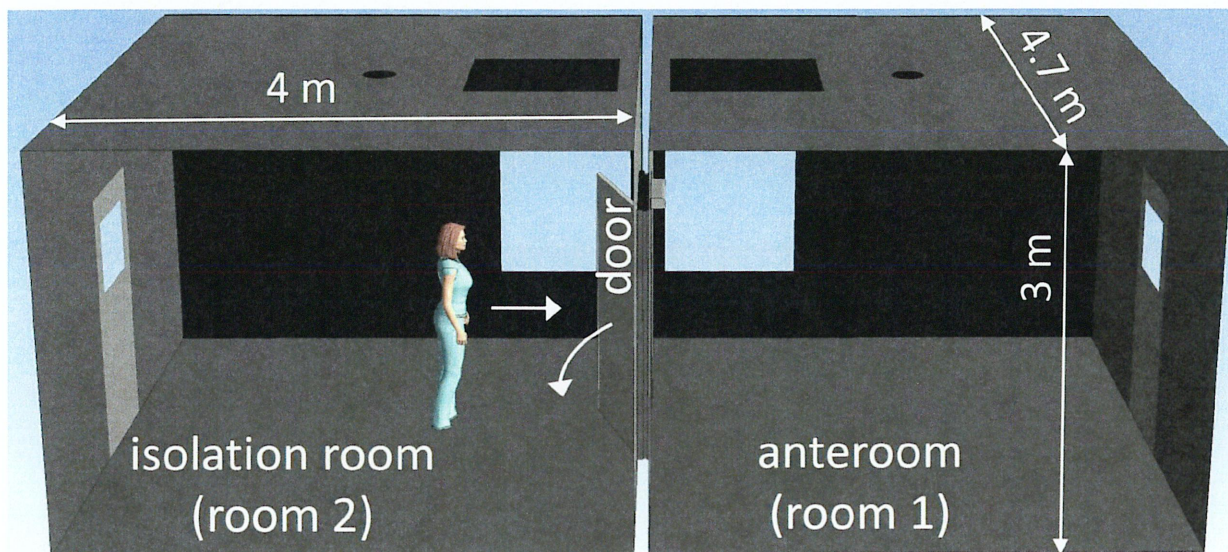


Fig 1. Timing of the test case. After an acceleration ramp, the manikin is moving with a steady velocity 1 m/s, ending in a deceleration ramp. The door moves with a steady angular velocity, different in the opening and closing phases.

doi:10.1371/journal.pone.0130667.g001

inevitable in this volume not only to resolve the air currents, but also because the immersed solid method applied uses the underlying mesh to resolve the surfaces of the moving objects. In the refined volume, a typical mesh element diameter was of the order of 1 cm, and the volumes of the finite volumes were 1.5×10^{-6} – 2.5×10^{-6} m³. Away from the refined area, the volumes increased to 1.5×10^{-3} – 4×10^{-3} m³. The discretization schemes used were second order backward Euler (transient scheme) and central difference (advection scheme). The two rooms together formed a closed system surrounded by wall boundary condition, and in the initial state the relative pressure as well as all the velocity components were set to zero everywhere. A 2 cm high gap was left below the door to avoid convergence problems in the beginning of the door-opening phase. This detail differed from the mock-up, where this gap was sealed by a moving seal that was automatically lifted when the door started to move. The two tracer gases

were modelled as passive scalars (CFX additional variables) and at zero time there was only one type of gas in one room.

The moving door and nurse were modelled by using immersed solid technique available in CFX, see [36, 30]. By using this method, no re-meshing is needed between the time steps. Instead, at each time step a check is made on whether the mesh elements lying in the trajectory of the moving object are located inside or outside of the object. If inside, the fluid element is forced to follow the course of the moving object. One should note that the immersed solid surface is not explicitly resolved, but its accuracy is dependent on the density of the underlying mesh.

The total CPU-time spent was approximately 94×10^6 s in a workstation equipped with 2.8 GHz Intel Xeon v2 processors. Therefore, use of parallel run is inevitable. On the other hand, the time step length of 2 ms used here is unnecessarily short most of the time, since the maximal Courant number stayed well below 1, mostly. Thus, the solver run can be carried out in a reasonable time by using effective parallelization and by using run-time adjustment of the time step, based on the Courant number.

Calculation of Air Volume Migration from Tracer Gas Measurements

The volume $\Delta V_{i \rightarrow j}$ of air migrating from room i to room j during the door and passage cycle can be measured if we mark the air in room i prior to the cycle. A standard method to do this is to release suitable tracer gas in the air in room i . Let us assume it is spread evenly throughout the room to have a uniform mass concentration ρ . After the door and passage cycle, if the air in room j is mixed with a fan, and the mass concentration of the tracer gas there *after the cycle* is measured and multiplied by the room volume, the migrated mass Δm of tracer gas is obtained. Then the volume of room i air that has escaped into room j is

$$\Delta V_{i \rightarrow j} = \frac{\Delta m}{\rho}.$$

Even in the absence of ventilation, the volume $\Delta V_{j \rightarrow i}$ of air migrated into the other direction, from room j to room i , does not need to be the same. This asymmetry comes from the fact that when the nurse passes through the doorway, the volume of air displaced by her travels in the opposite direction. By using two different tracer gases simultaneously, each dosed into different rooms, it is possible to independently measure the volumes of air passing through the doorway in each direction. In addition, these volumes can be calculated even if in the initial state the rooms are contaminated by tracer gas from the other room. This, in turn, enables measuring several door and passage cycles in succession, without a need to flush the rooms.

Let tracer gas 1 be initially dosed into room 1 and tracer 2 into room 2, but let us allow some mixing having taken place during preceding cycles. Then the average mass concentrations of the tracers in the other rooms *prior to the cycle* are nonzero, i.e. $\rho_{1, \text{room } 2}, \rho_{2, \text{room } 1} \neq 0$. Conservation of mass gives the net mass of tracer i escaped from room i as

$$\Delta m_{i, \text{room } i} = -\Delta m_{i, \text{room } j} = \Delta m_i = \rho_{i, \text{room } i} \Delta V_{i \rightarrow j} - \rho_{i, \text{room } j} \Delta V_{j \rightarrow i}.$$

Note that both mass concentrations are measured prior to the cycle, but calculation of the net migrated tracer masses Δm_i and Δm_j requires measurements of the concentrations after the cycle also, to get the differences. Writing the corresponding equation for tracer j and solving

the pair of equations for the migrated air volumes ΔV gives

$$\Delta V_{i \rightarrow j} = \frac{\rho_{j, \text{room } j} \Delta m_i + \rho_{i, \text{room } j} \Delta m_j}{\rho_{i, \text{room } i} \rho_{j, \text{room } j} - \rho_{i, \text{room } j} \rho_{j, \text{room } i}}. \quad (1)$$

The two tracer gases used in the measurements were N_2O and SF_6 , having characteristic infrared absorption bands well apart from each other and from the strongest bands of H_2O and CO_2 . Prior to their release into the rooms, they were diluted with clean air to prevent them from stratifying near the floor. The gases were initially dosed into different rooms, but mixing was taking place during repeated door and passage cycles, whereupon calculation of the AVMs from the measured concentrations was based on Eq (1). The concentrations of both the tracers in both the rooms were monitored by one gas analyzer (BK1302) taking the sample through sampling tubes that were perforated throughout their lengths. In addition, after the door had closed, the air in the rooms was mixed by fans. These actions were necessary to ensure the sample taken by the gas analyzer is representative of the overall conditions in the room. A third measure of confirmation was use of repeated measurements, as mentioned above. The door and passage cycle was repeated and measured 6 times (7 times in the case without passage). The results were scattered without a clear increasing or decreasing trend. To ensure proper flushing of the sampling tube, the gas analyzer took the sample from the exhaust tube of a more powerful pump. The photoacoustic sample cell of the analyzer was very small, with a volume of 3 cm^3 . It was flushed with a flow rate of $5 \text{ cm}^3/\text{s}$, giving a time constant less than one second. The flush time used was much longer than that, since there was no need to sample during the door cycle.

Calculation of Air Volume Migration from the Simulation

In CFD simulation initial mixing of the tracer gases is no concern, since in the initial state we are free to define $\rho_{1, \text{room } 2}, \rho_{2, \text{room } 1} = 0$. Eq (1) then simplifies to

$$\Delta V_{i \rightarrow j} = \frac{\Delta m_i}{\rho_{i, \text{room } i}}. \quad (2)$$

The migrated mass Δm_i of tracer i can be calculated at any instant of time t from the corresponding simulated time step by integrating the tracer mass concentration over the volume of the other room, i.e.:

$$\Delta m_i(t) = \iiint_{\text{room } j} \rho_i(\mathbf{r}, t) dV. \quad (3)$$

Inserting into Eq (2) gives $\Delta V_{i \rightarrow j}$ as a function of time. Thus, a LES simulation gives not only the total AVM, but its evolution in time as well. This enables us to examine, how rapidly the isolation room air is escaping at different stages of the door cycle. While real tracer gases are invisible, a time-resolved simulation provides a possibility to actually see the mixing of the airs from the two rooms. This is demonstrated in [S1 Video](#). In the video, the mass concentration of one of the tracer gases is coded by colours. Pure isolation room air is red and pure anteroom air deep blue. Any other colour is a mixture, 50%-50%-mixture being white.

Preparing Simulated Smoke Videos from a CFD LES Simulation

Since the tracer gases are invisible, they were replaced by smoke when visualizing the flow structures experimentally, in real-time. Smoke was then released into one of the rooms, where it stayed for a while, letting the temperature difference to vanish. The smoke was then neutrally buoyant. Since flow-driven transport phenomena dominate over diffusion, after the door-

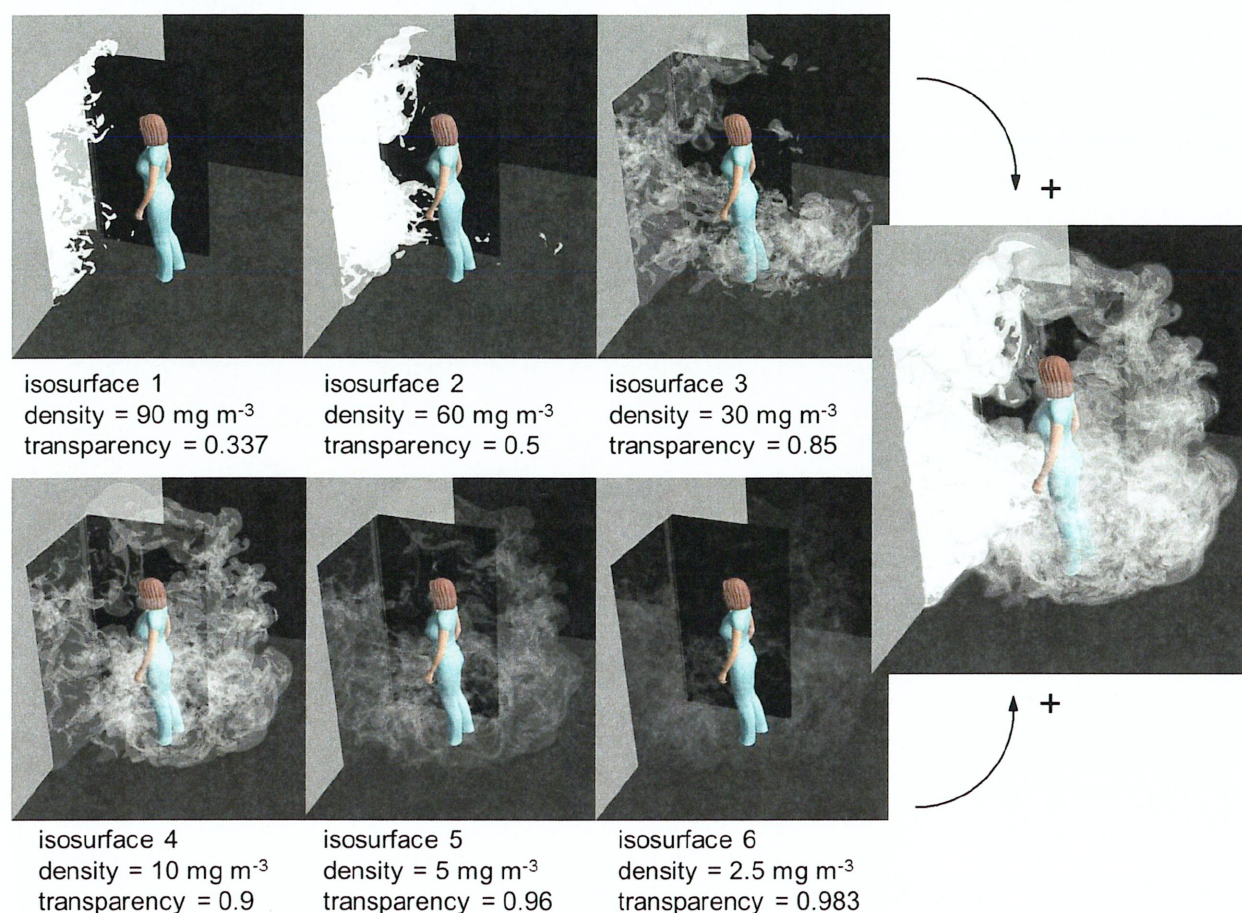


Fig 2. A generic method to prepare a simulated smoke visualization. Combining the six partially transparent isosurfaces of tracer gas concentration produces a simulated snapshot of a smoke experiment, as shown in the rightmost figure.

doi:10.1371/journal.pone.0130667.g002

opening smoke was carried into the other room by the air flows in the same manner as the tracer gases. Similarly, simulated smoke would be a useful illustrative tool to simulate the flow structures predicted by LES. Moreover, comparison of simulated smoke videos and real camcorder shots would be an interesting method to qualitatively validate the CFD results. Similar propagation of smoke and tracer gas makes it possible to use the same passive scalar to represent them both in the LES simulation.

When penetrating deeper into the smoke, into areas of larger concentration of smoke droplets, the light scattering becomes more and more effective. This means that the smoke becomes less and less transparent. This effect can be discretized by first dividing the smoke into a few nested volumes with different concentrations. Next, let us approximate that all the light scattering is taking place on the limiting surfaces between these volumes. Then only a few isosurfaces of tracer mass concentration need to be drawn and a negative correlation between the concentration and the transparency of the surface needs to be defined. This principle is illustrated in Fig 2. On the two rows on the left, six isosurfaces with different tracer concentrations and transparencies are drawn. The colour of all the isosurfaces equals the colour of the light source, and is white. The rightmost drawing of Fig 2 displays the complete smoke simulation, with all the six surfaces drawn simultaneously. If the same is repeated at time steps separated by 0.04 s

and they are shown with a frequency of 25 frames per second, we get a simulated smoke video in natural speed, easy to compare with an experimental one. An example is seen in [S2 Video](#). It is a simulation combining two separate smoke experiments. Smoke escaping from the isolation room into the anteroom is coloured white, whereas smoke going the opposite way is coloured yellow, corresponding to a yellow light source. This video is based on a single CFD LES simulation, having different passive scalars dosed into each room in the initial state (corresponding to two tracer gases or two separate smoke experiments). [Table 1](#) lists the isosurfaces and their transparencies, common to both passive scalars, used in preparing the video. There are no strict rules for the selection of these quantities. The only requirement is that different layers should be seen through each other in a natural-looking way. The video corresponds to situations where the rooms are entirely lit. It displays some basic flow structures, such as the jet through the gap below the door starting to open, the door vortices, and the wake of air the nurse is dragging behind her. It is comparable with the latter part of [S3 Video](#) by Tang et al. [22], showing the same features except that there is not a similar gap below the door.

Smoke is made visible by its ability to scatter light, necessitating a light source. Depending on the source, either a large volume, a strip, or only a narrow sheet of the smoke may be lit. When simulating the last-mentioned case, the isosurfaces reduce to isolines, since practically only a two-dimensional cross-section is lit. Then it is a better idea to plot a simple contour plot of the tracer (mass) concentration using a greyscale colour map. An example of this strategy is shown in [Fig 3](#). It shows an instantaneous greyscale map of the tracer gas concentration near a closing door. The higher the tracer concentration, the whiter the hue, simulating the smaller transparency or the more intense scattering of light by smoke droplets. The door vortex is clearly visible behind the door.

The method of greyscale maps described above is also useful in a situation, where a thick zone of smoke is lit with light whose direction of arrival is approximately perpendicular to a coordinate axis. It is also assumed the view direction is approximately parallel to the same coordinate axis. Then the light scattering can be easily discretized in the view direction by drawing several partially transparent greyscale maps above each other. An example is presented in [Fig 4](#). In the figure, four xy -oriented greyscale contour maps are drawn. Their transparency is increasing from bottom to top, so that when viewing from above, all the planes can be seen through each other. This creates an illusion of an illuminated horizontal thick zone of smoke. The method of contour maps is simpler and requires less computing than the method of isosurfaces, but is not suitable in a general case, where the line of sight is oblique.

Table 1. List of isosurfaces and their transparencies in the simulated smoke videos ([S2](#) and [S3 Videos](#)).

surface	tracer gas mass conc. [kg/m ³]	transparency
isosurface 1	60×10^{-6}	0.5
isosurface 2	30×10^{-6}	0.85
isosurface 3	10×10^{-6}	0.9
isosurface 4	5×10^{-6}	0.96
isosurface 5	2.5×10^{-6}	0.983
isosurface 6	1×10^{-6}	0.993

In the initial state the mass concentration of the tracer was 10^{-4} kg/m³ in the room it was dosed into.

doi:10.1371/journal.pone.0130667.t001



Fig 3. Simulation of smoke illuminated by a thin sheet of light. A greyscale contour map of the concentration of a passive scalar on a cross-sectional plane is equivalent to illuminating a thin sheet of smoke by white light.

doi:10.1371/journal.pone.0130667.g003

Results

Comparison of Simulated and Experimental Air Volume Migration

The most important result from this study is the volume of air migrating from the isolation room to the anteroom, in this single-hinged-door with/without manikin passage scenario. This quantity can be easily calculated by Eq (1) from a tracer gas measurement, or by integrating the amount of tracer gas 2 in room 1 in a simulation, see Eqs (2) and (3). A LES simulation provides more detailed information than measurements here in that it gives the AVM as a function of time.

The upper plot in Fig 5 shows the AVM(t) curve given by LES, together with the total AVMs obtained from a series of tracer gas measurements. A very intense flow through the doorway can be seen at the very beginning of the door-opening phase. This is due to the piston effect of the moving door, which in the beginning reduces the air volume in the isolation room. This effect causes a rapid counter-flow through the gap between the door and its frame. In the CFD simulation a 2 cm high gap was left below the door to avoid convergence problems. Another occasion of intense flow occurs when the nurse passes through the doorway. This is also the moment when the two AVM curves $\Delta V_{1 \rightarrow 2}(t)$ and $\Delta V_{2 \rightarrow 1}(t)$ separate, because the air displaced by the nurse moves from room 1 to room 2. The separation between the curves equals the volume of the nurse, which in this simulation was 0.070 m^3 (generally, with a good precision, one litre per one kilogram of mass). Finally, the AVM curve of Fig 5 ends up at a value of 1.54 m^3 , 20% (or 0.39 m^3) lower than the average of the repeated measurements at 1.93 m^3 . In another simulation, without the moving nurse, the corresponding result was 10% (or 0.15 m^3) too low (1.24 m^3 vs. 1.39 m^3), see [34] and the lower plot of Fig 5. This plot also shows how the amount of migrated air is growing steadily during the waiting period when no object is moving and the door stays open. This is in accordance with our experiments, which

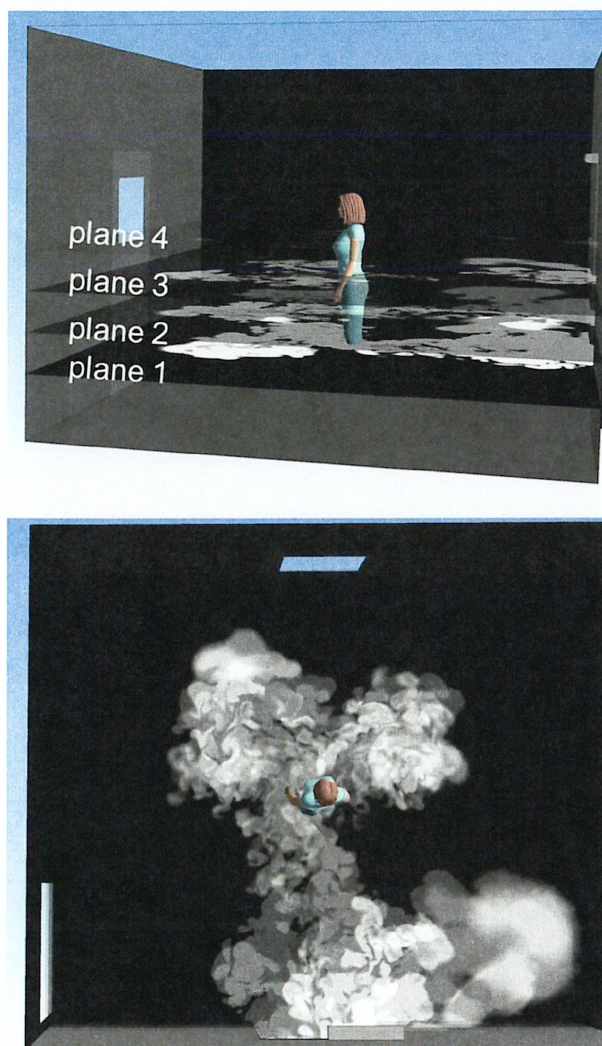


Fig 4. A simplified smoke simulation, viewable only from above. The upper figure shows four planar, greyscale contour maps of the tracer gas concentration at different heights. The lowest map is opaque, whereas the others are partially transparent. Together they simulate the smoke escaping from the isolation room, but only when viewed from above (lower figure).

doi:10.1371/journal.pone.0130667.g004

revealed that the AVM grows steadily over an extended period of time during the hold-open phase, see Kalliomäki et al. [28, 35].

From the lower plot of Fig 5, the total simulated volume of air migrated in the door-opening phase (duration 3 s) is 0.412 m^3 . In the door-closing phase the flow continued at almost unchanged rate, the volume of air migrated being 0.327 m^3 . These volumes total to approximately 0.74 m^3 by door-pumping alone, with the hold-open phase omitted. Including a hold-open time of 1 s, probably used by Kiel and Wilson [33], would increase the AVM to approximately 0.81 m^3 . The analytical formula introduced by Kiel and Wilson would give $\text{AVM} = 2.3 \text{ m}^2 \text{ s } U_d = 0.68 \text{ m}^3$, which is rather near the simulated value. Here, one should note that in our case the door-closing time was longer (5.4 s) than the opening time (3 s), while they were obviously identical in the experiments of Kiel and Wilson. Since the flow rate stays almost constant during the closing phase, we can approximate that a closing time of 3 s would have resulted in air volume of

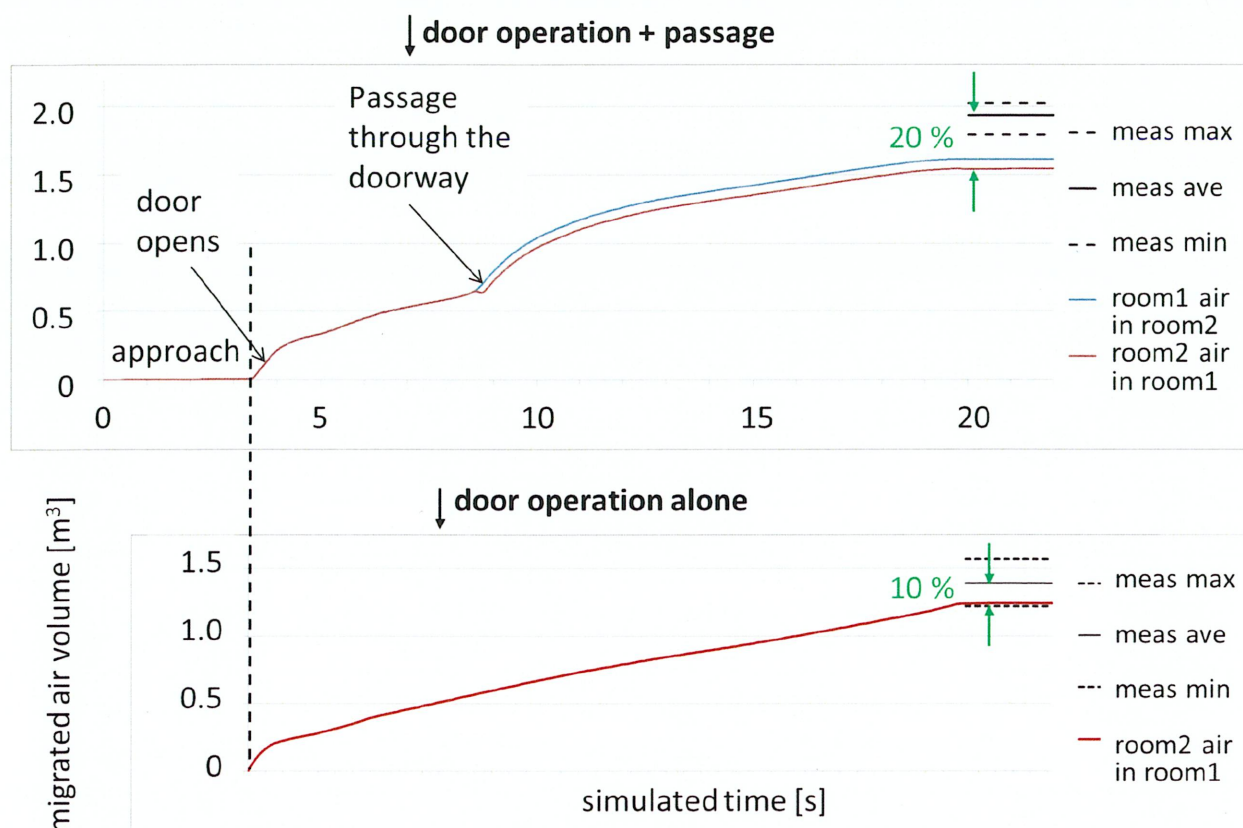


Fig 5. Air volume migrated: CFD LES compared to measurements. Time evolution of AVM as given by LES simulation during the door operation cycle with (top) and without (bottom) passage. The corresponding total values, as given by measurements, are also shown. The range of repetition measurements has been indicated by dashed lines.

doi:10.1371/journal.pone.0130667.g005

$3/5.4 \times 0.327 \text{ m}^3 = 0.182 \text{ m}^3$ migrated during the door-closing. Then the total AVM would be 0.66 m^3 , which is almost exactly the same as the result by Kiel and Wilson. One should however note that the door used by Kiel and Wilson was an exterior door, not an interior door as in our case, and their data were rather scattered. In addition, Kiel and Wilson warn in their paper that their result for AVM due to door-pumping is not properly non-dimensionalized for the door size, and is therefore only valid for width W near 0.91 m used in their experiments. In our case W is 24% larger than this.

The difference between the final AVM with combined door operation and passage on the other hand, and door operation alone on the other hand, gives the additional effect of a human passage on the total AVM. It is not, of course, equivalent to the AVM due to human passage in the absence of the door operation. The value of this difference was 0.54 m^3 in the measurements and 0.30 m^3 in the simulations. Our measurements with a sliding door, with much less disturbance by the door itself, resulted in additional AVM of $0.92 \text{ m}^3 - 0.56 \text{ m}^3 = 0.36 \text{ m}^3$ generated by the passage [28, 35]. This suggests that the human wake is an important agent in air transport. Concerning the relative proportion of the air volume of one room, migrating into the other room, Choi and Edwards [29] obtained a percentage of 2.5 in the case of walking speed 1 m/s and in the absence of the door. This means an AVM of 0.98 m^3 . This result was obtained 6 s after the human stopped, which makes it approximately comparable with the final AVM in our case. Also, the human stopped at 3.2 m from the doorway, while in the present

study it stopped already at the distance of 2 m. Taking into account the deceleration ramp in our simulation, the time from the moment the nurse passes the doorway to the moment the door is half-closed is 8.45 s. In the paper of Choi and Edward, the time from the moment the human passes the doorway to the moment the AVM is measured, is 9.2 s. Thus, the time of influence of the wake is nearly the same in both simulations. However, their rooms and doorway were smaller than in our study (39.2 m^3 against 56.4 m^3 and 1.74 m^2 against 2.23 m^2). Tang et al. [21] estimated a range of values for the flux of the wake induced by a moving human, being $0.08\text{--}0.23 \text{ m}^3/\text{s}$, though this estimate does not appear to take into consideration how the flux behaves over time during the passage and after the nurse has stopped moving.

According to the above, it is obvious that the AVM due to the human wake varies considerably depending on the geometrical details and on the details of the door operation. In case of a hinged door, the direction of the passage might also be crucial. In our case the nurse was moving against the movement of the opening door, and the effect of the passage was to reinforce the air migration. The situation might be different to the other direction [35]. Thus, one should be cautious to give a simple and generic rule of the effect of human wake on the AVM.

It is common in fluid dynamics to present results in a more general form by grouping two or more parameters into one or more non-dimensional variables. If we can state results by using such variables, they are applicable to any set of numerical values of the individual parameters. An obvious example is grouping flow velocity, duct diameter, and viscosity into Reynolds number. Since a large set of data with varying parameter values is required to test such general relations, the results are presented here in terms of original dimensional variables, such as simulated time and migrated air volume in Fig 5. A set of varied door and passage cycles was tested in the experimental section of our study [35].

The purpose of this paper is to report a CFD LES simulation in one example case, to aid in assessing the accuracy of the CFD approach and to introduce the computer modeled, multi-layered, smoke videos. The door parameters varied in the laboratory experiments were opening-time, hold-open time, closing-time, and opening-angle. It was noted then that reducing the opening-speed (in the absence of ventilation) resulted in larger AVM, or that the effect of increased duration overrode the effect of faster door movement. Moreover, without passage the air escape through the doorway continued at nearly constant speed up to the longest hold-open time tested (25 s). A similar effect has been found by Hathway et al. [37] who studied doorway flows generated by a single hinged-door in a small-scale water tank model. The effect of opening angle (90° vs 45° tested) was smaller, but clearly detectable. By contrast, the effect of a 2°C temperature difference between the two rooms resulted in 41% increase in the AVM in the case used in the CFD simulation [35].

Comparison of Experimental and Simulated Flow Patterns

In order to visualize the air flows through the doorway, smoke was released in one of the rooms, and the smoke eddying into the other room was illuminated and videoed. The characteristic flow patterns near the doorway were found to be well discerned by illuminating a horizontal strip at the centre of the door, and shooting a video from above, through a ceiling window. Using the methods described above, corresponding simulated smoke videos were prepared and validated against camcorder shots. Fig 6 shows smoke travelling from the anteroom to the isolation room. Only the height interval from 0.6 m to 1.4 m above the floor is illuminated. The opening door vortex is just colliding with the nurse standing in front of the opening door. This figure is one frame from S3 Video, displaying the camcorder shot and the simulated (isosurface method) smoke as a function of time. Both the experiment and the simulation reveal the same principal flow features:

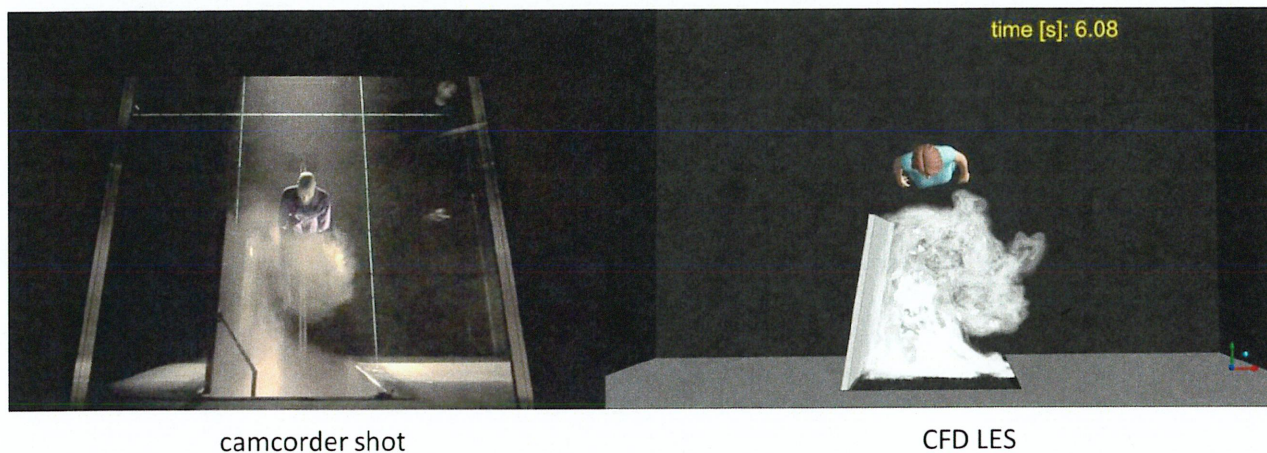


Fig 6. Smoke experiment in the isolation room side. Experimental (on the left) and simulated (on the right) smoke visualizations of the nurse exiting the isolation room. This figure is one frame of [S3 Video](#), showing the flow structures as a function of time. Note that only a certain height interval is lit.

doi:10.1371/journal.pone.0130667.g006

- An opening door vortex develops and separates from the door, as it swings open.
- After the nurse passage, a thick cloud of smoke pours through the door.
- A closing-door vortex develops behind the door, as it begins to close.
- After the door has closed, the stem of the vortex drifts to the right.
- The stem hits the side wall and continues along it.

The same phenomena can be seen in the water model experiments (see the latter part of [S3 Video](#) in [22]), but since the entire model is illuminated, the dye above the door blocks the sight to the closing door vortex.

In [Fig 7](#) smoke has been dosed into the isolation room, and the anteroom side is shown. This time the simulated smoke has been generated by using the simplified method with four contour surfaces, as demonstrated in [Fig 4](#). Again, the figure is one frame out of a time-resolved presentation, [S4 Video](#). The main flow features, visible both in the experiment and in the simulation are:

- At the beginning of the door-opening motion, there is a rapid burst of smoke far ahead of the door.
- Soon after the door has started to open, the major air flow turns diagonally to the right.
- The nurse trails a wake of smoke behind her as she moves forward.
- When the nurse stops, the wake catches up and collides with her, splitting and passing to both sides around her, and starting to spread sideways.

Perhaps the most eye-catching difference is that in the experimental smoke video the opening door vortex extends further away from the doorway and is shooting more smoke on the left side of the room. This could be one reason for the difference between the measured and the modelled AVM. On the other hand, in the water model experiment by Tang et al. (the latter part of [S3 Video](#) in [22]), the left side of the anteroom is devoid of smoke during door operation and passage, just as in the simulation.

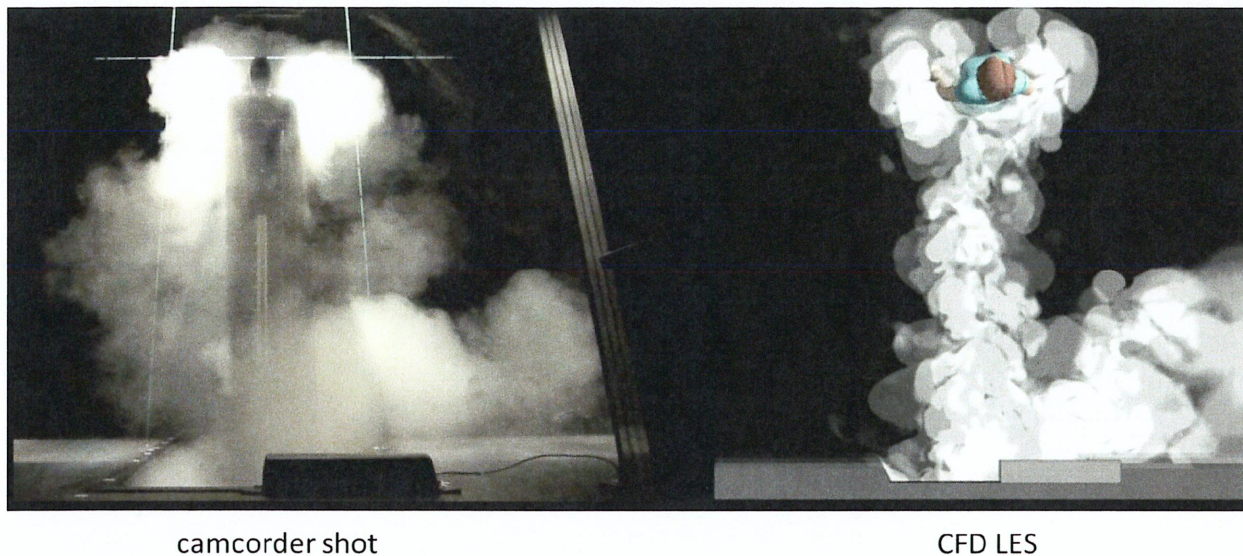


Fig 7. Smoke experiment in the anteroom side. Experimental smoke visualization as compared with simulated smoke drawn by the method of stacked contour maps. This figure is one frame of [S4 Video](#). Again, a certain height interval alone is being lit.

doi:10.1371/journal.pone.0130667.g007

Discussion

The simulated amount of air escaped from the isolation room was 20% smaller than the average in the tracer gas experiments. On the other hand, the simulated amount with a mere door cycle without the nurse/manikin passage was only 10% smaller than the corresponding experimental value. This suggests that simulation of the moving door and moving nurse both contribute a 10% relative error to the final simulated AVM. These were the first tests, and the results can probably be still improved by improving the accuracy of the computation and also of the geometry.

The accuracy of the time-marching, when measured by the Courant number, was good. The maximal Courant number stayed well below one almost all the time. There were only two occasions of noteworthy excess of 1. The first occasion was just in the beginning of the door-opening, where the maximal Courant number momentarily rose to 5.68. Another occasion was the moment of door-closing, when the maximal Courant number reached the value 4.12. These values are not critical, and shortening the time step at these instances does not alter the results significantly, as shown by [Fig 8](#). A recommended test of spatial resolution is to rerun the simulation by using a denser mesh. However, this was not practical due to the large computation time. Also, because of memory limitations, significant mesh refinement would not have been possible.

Part of the differences between experiments and simulation could be explained by inaccuracies in the modelled geometry. These include the gap below the door in the CFD simulation and differences in the real and simulated manikin. In the simulation, the under-door gap was present all the time, whereas in the experiments this gap was sealed until the door started to open. This discrepancy affects the pressure pulse generated when the door starts to push the air in the isolation room. This piston effect is not present in case of a sliding door, which is the next case we are modelling, thus enabling an estimate of its significance and impact of this effect. The nurse used in the simulation was a commercial CAD model of a female, not an exact model of the manikin used in the experimental measurements. The outfit worn by the

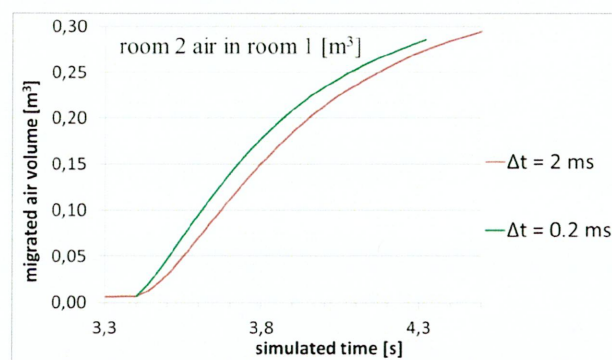


Fig 8. A test using a shorter time step. Green curve shows the result of shortening the time step by a factor of 10 at the beginning of door-opening. The AVM(t)-curve first rises 0.028 m³ above the original curve, but after that begins to approach it again.

doi:10.1371/journal.pone.0130667.g008

CFD-modelled human was much more streamlined than the robe worn by the manikin in the experiments. Moreover, the wheeled cart under the manikin was not modelled.

In order to resolve the effects of door operation and passage, the basic case simulated in this paper did not contain ventilation. The effect of ventilation on the pathogen transmission is reviewed in the WHO guideline [25], based on 65 selected studies. It was obvious that the information about the impact of different types of ventilation on the reduction of infectious risks is insufficient. The main findings were that while insufficient ventilation increases the disease transmission and high ventilation rates could decrease it, there is no information that droplet-transmitted infections can be reduced by increasing ventilation rate. On the other hand, there is not enough data to define a minimum ventilation flow rate against infections through droplet nuclei (concluded also by Li et al [38]).

Concerning the ventilation strategies in isolation rooms, displacement ventilation is not recommended. The reason is that the large vertical temperature gradient characteristic to the displacement strategy can result in stratification of the exhaled air at some level [39, 24], and increase cross-transmission risks. Buoyancy also gives more time to the droplets to evaporate and become airborne.

A very large air flow rate without creating a draughty environment can be attained by using downward ventilation with large supply area [24]. Guidelines for isolation rooms do not recommend any particular ventilation strategy, but require keeping the room at negative pressure differential [40]. Kim and Augenbroe [41] suggest satisfying this by adaptive VAV (Variable Air Volume) operation, normally maintaining a low negative pressure differential, but temporarily inducing a higher value prior to door operation, to reduce energy consumption. As demonstrated by Adams et al [42], containment failure during door operation and passage can be significantly reduced by applying pressure difference. Even though the pressure differential immediately disappears when the door is opened, the supply and exhaust air flow differential, used to generate the underpressure in the isolation room, remains and works against the flow escaping from the isolation room.

In summary, if available, the use of modern workstations and parallel processing allows a time-resolved LES flow simulation to be a feasible method for room-scale flow modelling. The use of LES is attractive, since it enables the air flow features to be made visible, e.g. by using the simulated smoke method, as introduced in this study. Even though the present case was a simple, isothermal basic case without ventilation, the addition of ventilation would not be difficult and would not require much additional computing. In fact, this would be a natural

continuation of this study. The effect of temperature differences between the rooms may be even greater than that of ventilation, and its effect could also be easily simulated. Finally, the thermal plume of the nurse (when not moving) has not been taken into account in this simulation, but this could also be simulated and should be taken into account in future models.

Supporting Information

S1 Video. Mixing of isolation room air and anteroom air. In this simulated video, featuring vertical cross-sectional plane in the middle of the rooms, (mass) concentration of one of the passive scalar variables is colour coded. In the initial state, isolation room (on the left) air is red and anteroom (on the right) air is deep blue. Any other colour is a mixture, equal distribution being white.

(MP4)

S2 Video. A simulated smoke video combining two smoke experiments. This simulation is prepared by using the method of isosurfaces as detailed in the text. It combines two separate smoke experiments by using two passive scalars, originally dosed into different rooms. The smoke escaping from the isolation room is illuminated by white light, while the smoke going the other way (into the isolation room) is illuminated by yellow light.

(MP4)

S3 Video. Experimental vs simulated smoke visualization as seen from above the isolation room. This combined video offers an opportunity to compare a real (left) and simulated (right) smoke video. In both videos only the height interval from 0.6 m to 1.4 m is lit to bring out the most interesting flow features.

(MP4)

S4 Video. Experimental vs simulated smoke visualization as seen from above the anteroom. This combined video has been prepared by using the method of planar contour maps, and works only when viewed from above. Again, only the height interval from 0.6 m to 1.4 m is lit.

(MP4)

Author Contributions

Conceived and designed the experiments: HK JWT. Performed the experiments: PK. Analyzed the data: PES PK. Contributed reagents/materials/analysis tools: PES. Wrote the paper: PES. Designed the methods to obtain simulated smoke videos: PES.

References

1. Wong TW, Lee CK, Tam W, Lau JT, Yu TS, Lui SF, et al. Outbreak Study Group. Cluster of SARS among medical students exposed to single patient, Hong Kong. *Emerg Infect Dis*. 2004 Feb; 10(2):269–76. PMID: [15030696](#)
2. Yu IT, Li Y, Wong TW, Tam W, Chan AT, Lee JH, et al. Evidence of airborne transmission of the severe acute respiratory syndrome virus. *N Engl J Med*. 2004 Apr 22; 350(17):1731–9. PMID: [15102999](#)
3. Li Y, Huang X, Yu IT, Wong TW, Qian H. Role of air distribution in SARS transmission during the largest nosocomial outbreak in Hong Kong. *Indoor Air*. 2005 Apr; 15(2):83–95. PMID: [15737151](#)
4. Li Y, Duan S, Yu IT, Wong TW. Multi-zone modeling of probable SARS virus transmission by airflow between flats in Block E, Amoy Gardens. *Indoor Air*. 2005 Apr; 15(2):96–111. PMID: [15737152](#)
5. Booth TF, Kournikakis B, Bastien N, Ho J, Kobasa D, Stadnyk L, et al. Detection of airborne severe acute respiratory syndrome (SARS) coronavirus and environmental contamination in SARS outbreak units. *J Infect Dis*. 2005 May 1; 191(9):1472–7. PMID: [15809906](#)

6. Yu IT, Qiu H, Tse LA, Wong TW. Severe acute respiratory syndrome beyond Amoy Gardens: completing the incomplete legacy. *Clin Infect Dis*. 2014 Mar; 58(5):683–6. doi: [10.1093/cid/cit797](https://doi.org/10.1093/cid/cit797) PMID: [24319085](https://pubmed.ncbi.nlm.nih.gov/24319085/)
7. Lindsley WG, Blachere FM, Thewlis RE, Vishnu A, Davis KA, Cao G, et al. Measurements of airborne influenza virus in aerosol particles from human coughs. *PLoS One*. 2010 Nov 30; 5(11):e15100. doi: [10.1371/journal.pone.0015100](https://doi.org/10.1371/journal.pone.0015100) PMID: [21152051](https://pubmed.ncbi.nlm.nih.gov/21152051/)
8. Lindsley WG, Pearce TA, Hudnall JB, Davis KA, Davis SM, Fisher MA, et al. Quantity and size distribution of cough-generated aerosol particles produced by influenza patients during and after illness. *J Occup Environ Hyg*. 2012; 9(7):443–9. doi: [10.1080/15459624.2012.684582](https://doi.org/10.1080/15459624.2012.684582) PMID: [22651099](https://pubmed.ncbi.nlm.nih.gov/22651099/)
9. Lednicky JA, Loeb JC. Detection and Isolation of Airborne Influenza A H3N2 Virus Using a Sioutas Personal Cascade Impactor Sampler. *Influenza Res Treat*. 2013; 2013:656825. doi: [10.1155/2013/656825](https://doi.org/10.1155/2013/656825) PMID: [24224087](https://pubmed.ncbi.nlm.nih.gov/24224087/)
10. Bischoff WE, Swett K, Leng I, Peters TR. Exposure to influenza virus aerosols during routine patient care. *J Infect Dis*. 2013 Apr; 207(7):1037–46. doi: [10.1093/infdis/jis773](https://doi.org/10.1093/infdis/jis773) PMID: [23372182](https://pubmed.ncbi.nlm.nih.gov/23372182/)
11. Lindsley WG, Noti JD, Blachere FM, Thewlis RE, Martin SB, Othumpangat S, et al. Viable influenza A virus in airborne particles from human coughs. *J Occup Environ Hyg*. 2015; 12(2):107–13. doi: [10.1080/15459624.2014.973113](https://doi.org/10.1080/15459624.2014.973113) PMID: [25523206](https://pubmed.ncbi.nlm.nih.gov/25523206/)
12. Tellier R. Review of aerosol transmission of influenza A virus. *Emerg Infect Dis*. 2006 Nov; 12(11):1657–62. PMID: [17283614](https://pubmed.ncbi.nlm.nih.gov/17283614/)
13. Lemieux C, Brankston G, Gitterman L, Hirji Z, Gardam M. Questioning aerosol transmission of influenza. *Emerg Infect Dis*. 2007 Jan; 13(1):173–4; author reply 174–5. PMID: [17370541](https://pubmed.ncbi.nlm.nih.gov/17370541/)
14. Brankston G, Gitterman L, Hirji Z, Lemieux C, Gardam M. Transmission of influenza A in human beings. *Lancet Infect Dis*. 2007 Apr; 7(4):257–65. PMID: [17376383](https://pubmed.ncbi.nlm.nih.gov/17376383/)
15. Tang JW, Li Y. Transmission of influenza A in human beings. *Lancet Infect Dis*. 2007 Dec; 7(12):758; author reply 761–3. PMID: [18045554](https://pubmed.ncbi.nlm.nih.gov/18045554/)
16. Tellier R. Aerosol transmission of influenza A virus: a review of new studies. *J R Soc Interface*. 2009 Dec 6; 6 Suppl 6:S783–90. doi: [10.1098/rsif.2009.0302.focus](https://doi.org/10.1098/rsif.2009.0302.focus) PMID: [19773292](https://pubmed.ncbi.nlm.nih.gov/19773292/)
17. Nikitin N, Petrova E, Trifonova E, Karpova O. Influenza virus aerosols in the air and their infectiousness. *Adv Virol*. 2014; 2014:859090. doi: [10.1155/2014/859090](https://doi.org/10.1155/2014/859090) PMID: [25197278](https://pubmed.ncbi.nlm.nih.gov/25197278/)
18. Seto WH. Airborne transmission and precautions: facts and myths. *J Hosp Infect*. 2014 Dec 13. pii: S0195-6701(14)00370-3. doi: [10.1016/j.jhin.2014.11.005](https://doi.org/10.1016/j.jhin.2014.11.005) [Epub ahead of print]
19. Center for Infectious Disease Research and Policy (CIDRAP): <http://www.cidrap.umn.edu/news-perspective/2014/09/commentary-health-workers-need-optimal-respiratory-protection-ebola>
20. Tang JW, Eames I, Li Y, Taha YA, Wilson P, Bellingan G, et al. Door-opening motion can potentially lead to a transient breakdown in negative-pressure isolation conditions: the importance of vorticity and buoyancy airflows. *J Hosp Infect*. 2005; 61:283–286. PMID: [16253388](https://pubmed.ncbi.nlm.nih.gov/16253388/)
21. Tang JW, Li Y, Eames I, Chan PKS, Ridgway GL. Factors involved in the aerosol transmission of infection and control of ventilation in healthcare premises. *J Hosp infect*. 2006; 64:100–114. PMID: [16916564](https://pubmed.ncbi.nlm.nih.gov/16916564/)
22. Tang JW, Nicolle A, Pantelic J, Klettner CA, Su R, Kalliomäki P, et al. Different types of door-opening motions as contributing factors to containment failures in hospital isolation rooms. *PLoS ONE* 2013; 8: e66663. doi: [10.1371/journal.pone.0066663](https://doi.org/10.1371/journal.pone.0066663) PMID: [23826109](https://pubmed.ncbi.nlm.nih.gov/23826109/)
23. Fernstrom A, Goldblatt M. Aerobiology and Its Role in the Transmission of Infectious Diseases. *J Pathog*. 2013; 1–12. doi: [10.1155/2013/493960](https://doi.org/10.1155/2013/493960)
24. Nielsen PV. Air Distribution Systems and Cross-Infection Risk in the Hospital Sector. In: *Proceedings of Ventilation 2012, The 10th International Conference on Industrial Ventilation*; 2012 Sep 17–19 Paris, France.
25. Atkinson J, Chartier Y, Pessoa-Silva CL, Jensen P, Li Y, Seto WH, editors. *Natural Ventilation for Infection Control in Health-Care Settings*. WHO guidelines 2009.
26. Morawska L, Johnson GR, Ristovski ZD, Hargreaves M, Mengersen K, Corbett S, et al. Size distribution and sites of origin of droplets expelled from the human respiratory tract during expiratory activities. *J Aerosol Sci*. 2009; 40:256–269.
27. Papineni RS, Rosenthal FS. The size distribution of droplets in the exhaled breath of healthy human subjects. *J Aerosol Med*. 1997; 10:105–116. PMID: [10168531](https://pubmed.ncbi.nlm.nih.gov/10168531/)
28. Kalliomäki P, Saarinen P, Tang JW, Koskela H. Airflow patterns through a single hinged and a sliding door in hospital isolation room. In: *Proceedings of Indoor Air 2014, 13th International Conference on Indoor Air Quality and Climate*; 2014 July 7–12; Hong Kong, China.

29. Choi JI, Edwards JR. Large eddy simulation and zonal modeling of human-induced contaminant transport. *Indoor Air*. 2008; 18:233–249. doi: [10.1111/j.1600-0668.2008.00527.x](https://doi.org/10.1111/j.1600-0668.2008.00527.x) PMID: [18422965](https://pubmed.ncbi.nlm.nih.gov/18422965/)
30. Choi JI, Oberoi RC, Edwards JR, Rosati JA. An immersed boundary method for complex incompressible flows. *J Comput. Phys.* 2007; 224:757–784.
31. Choi JI, Edwards JR. Large-eddy simulation of human-induced contaminant transport in room compartments. *Indoor Air*. 2012; 22:233–249.
32. Shih YA, Chiu CC, Wang O. Dynamic airflow simulation within an isolation room. *Build Environ*. 2007; 42:3194–3209.
33. Kiel DE, Wilson DJ. Combining door swing pumping with density driven flow. *ASHRAE Trans II* 1989; 95:590–599.
34. Saarinen P, Kalliomäki P, Tang JW, Koskela H. Air leakage through isolation room doorway – measurements and CFD simulations. In: *Proceedings of Indoor Air 2014, 13th International Conference on Indoor Air Quality and Climate*; 2014 July 7–12; Hong Kong, China.
35. Kalliomäki P, Saarinen P, Tang JW, Koskela H. Airflow patterns through single hinged and sliding doors in hospital isolation rooms. *Int J Vent*. Forthcoming 2015.
36. Mittal R, Iaccarino G. Immersed Boundary Methods. *Annu Rev Fluid Mech*. 2005; 37: 239–261.
37. Hathway A, Papakonstantis I, Konuah AB, Brevis W. Towards understanding the role of human activity on indoor air flows: A case study of door motion based on both field and experimental activities. In: *Proceedings of Indoor Air 2014, 13th International Conference on Indoor Air Quality and Climate*; 2014 July 7–12; Hong Kong, China.
38. Li Y, Leung GM, Tang JW, Yang X, Chao CYH, Lin JZ, et al. Role of ventilation in airborne transmission of infectious agents in the built environment—a multidisciplinary systematic review. *Indoor Air*. 2007 Feb; 17(1):2–18. PMID: [17257148](https://pubmed.ncbi.nlm.nih.gov/17257148/)
39. Olmedo I, Nielsen PV, Ruiz de Ana M, Jensen RL, Grzelecki P. Distribution of exhaled contaminants and personal exposure in a room using three different air distribution strategies. *Indoor Air*. 2012 Feb; 22(1):64–76. doi: [10.1111/j.1600-0668.2011.00736.x](https://doi.org/10.1111/j.1600-0668.2011.00736.x) PMID: [21815935](https://pubmed.ncbi.nlm.nih.gov/21815935/)
40. American Society of Heating, Refrigerating and Air-Conditioning Engineers, Inc.: HVAC design manual for hospitals and clinics, ISBN 1-931862-26-5. ASHRAE, Atlanta, USA. 2013.
41. Kim HK, Augenbroe G. Decision support for choosing ventilation operation strategy in hospital isolation rooms: A multi-criterion assessment under uncertainty. *Build Environ*. 2013; 60:305–318.
42. Adams NJ, Johnson DL, Lynch RA. The effect of pressure differential and care provider movement on airborne infectious isolation room containment effectiveness. *Am J Infect Control*. 2011; 39:91–97. doi: [10.1016/j.ajic.2010.05.025](https://doi.org/10.1016/j.ajic.2010.05.025) PMID: [20864218](https://pubmed.ncbi.nlm.nih.gov/20864218/)